

CLASH-VLT: Enhancement of (O/H) in $z = 0.35$ RX J2248–4431 cluster galaxies[★]

B. I. Ciocan, C. Maier, B. L. Ziegler, and M. Verdugo

University of Vienna, Department of Astrophysics, Tuerkenschanzstrasse 17, 1180 Vienna, Austria
e-mail: bianca-iulia.ciocan@univie.ac.at

Received 16 September 2019 / Accepted 22 November 2019

ABSTRACT

Aims. Gas-phase metallicities offer insight into the chemical evolution of galaxies as they reflect the recycling of gas through star formation and galactic inflows and outflows. Environmental effects such as star-formation quenching mechanisms play an important role in shaping the evolution of galaxies. Clusters of galaxies at $z < 0.5$ are expected to be the sites where environmental effects can be clearly observed with present-day telescopes.

Methods. We explored the Frontier Fields cluster RX J2248–443 at $z = 0.348$ with VIMOS/VLT spectroscopy from CLASH-VLT, which covers a central region corresponding to almost 2 virial radii. The fluxes of [OII] $\lambda 3727$, H β , [OIII] $\lambda 5007$, H α and [NII] $\lambda 6584$ emission lines were measured allowing the derivation of (O/H) gas metallicities, star formation rates based on extinction-corrected H α fluxes, and contamination from active galactic nuclei. We compared our sample of cluster galaxies to a population of field galaxies at similar redshifts.

Results. We use the location of galaxies in projected phase-space to distinguish between cluster and field galaxies. Both populations follow the star-forming sequence in the diagnostic diagrams, which allow the ionising sources in a galaxy to be disentangled, with only a low number of galaxies classified as Seyfert II. Both field and cluster galaxies follow the “main sequence” of star-forming galaxies, with no substantial difference observed between the two populations. In the mass–metallicity (MZ) plane, both high-mass field and cluster galaxies show comparable (O/H)s to the local SDSS MZ relation, with an offset of low-mass galaxies ($\log(M/M_{\odot}) < 9.2$) towards higher metallicities. While both the metallicities of “accreted” ($R < R_{500}$) and “infalling” ($R > R_{500}$) cluster members are comparable at all masses, the cluster galaxies from the “mass complete” bin (which is the intermediate mass bin in this study: $9.2 < \log(M/M_{\odot}) < 10.2$), show more enhanced metallicities than their field counterparts by a factor of 0.065 dex with a $\sim 1.8\sigma$ significance. The intermediate-mass field galaxies are in accordance with the expected (O/H)s from the fundamental metallicity relation, while the cluster members deviate strongly from the model predictions, namely by a factor of ~ 0.12 dex. The results of this work are in accordance with studies of other clusters at $z < 0.5$ and favour the scenario in which the hot halo gas of low- and intermediate-mass cluster galaxies is removed due to ram pressure stripping, leading to an increase in their gas-phase metallicity.

Key words. Galaxy: evolution – galaxies: clusters: individual: RX J2248–443 – galaxies: star formation – galaxies: abundances

1. Introduction

The chemical abundances of galaxies are an important tool to study galaxy evolution, as they reflect the complex interplay between star formation, gas outflows through winds and supernovae, and galactic gas inflows. A large number of studies concentrating on galaxies in the local universe have shown that there is a tight correlation of 0.1 dex between the stellar mass of a galaxy and its gas phase metallicity, giving rise to the so-called mass–metallicity relation (MZR): the more massive the galaxy is, the higher its (O/H) oxygen abundance will be (e.g. Tremonti et al. 2004; Kewley & Ellison 2008). There is also good evidence that this MZR evolves with redshift: for a given mass, gas-phase metallicities are higher at lower redshifts (e.g. Zahid et al. 2013; Pérez-Montero et al. 2013; Maier et al. 2015). Based on extensive SDSS data, it has been claimed that gas phase metallicities correlate with other galactic parameters as well, such as the star formation rate (SFR; e.g. Mannucci et al. 2010). Salim et al. (2014) has shown that for local galaxies the (O/H) anti-correlates with the SFR, regardless of the metallicity

or SFR calibrators used. Observations have also demonstrated that out to $z \sim 2$ there exists a “main sequence” (MS) of star-forming (SF) galaxies in which the SFR is closely linked with the stellar mass of a galaxy (e.g. Brinchmann et al. 2004; Daddi et al. 2007; Whitaker et al. 2014). The MS has a characteristic specific SFR (sSFR) that declines weakly with the stellar mass as: $\text{sSFR} \propto m_{\text{star}}^{\beta}$ with $\beta \sim -0.24$ (Renzini & Peng 2015). Observations also demonstrate that the sSFR strongly evolves with redshift on the MS as: $\text{sSFR} \propto (1+z)^3$. For a given mass, the SFR has been decreasing at a steady rate by a factor of approximately 20 from $z = 2$ to $z = 0$ (e.g. Elbaz et al. 2007; Peng et al. 2010).

An explanation of the origin of the MZR and SF MS has been summarised by Lilly et al. (2013), and is known as the bathtub model. The SFR in this gas-regulated model is closely linked to the mass of the gas reservoir in the galaxy, which is in turn regulated by galactic gas inflows and outflows. The model produces an implicit dependency of the gas-phase metallicity on both the stellar mass and the SFR, giving birth to the so-called fundamental metallicity relation: $Z(M^*, \text{SFR})$, which is believed to be epoch-invariant (e.g. Mannucci et al. 2010).

The evolution of galaxies is known to be internally regulated by the build up of the stellar mass and externally influenced

[★] Based on observations obtained at the European Southern Observatory (ESO) Very Large Telescope (VLT), Paranal, Chile; ESO large program 186.A-0798.

by the environment in which they reside; e.g. Peng et al. (2012). Observations have shown that the physical properties, such as the SFR, colour, morphology, metallicity, and active galactic nucleus (AGN) fraction, of galaxies residing in a high-density environment can differ from the properties of isolated field galaxies (e.g. Dressler 1980; Balogh et al. 2004; Kauffmann et al. 2004; Ellison et al. 2008). A plausible mechanism which offers an explanation for the observed differences between the field and cluster populations (e.g. Dressler 1980) is the quenching of star formation when the galaxy is accreted onto the cluster. Cluster-specific processes such as the hydrodynamical interaction between the hot intracluster medium (ICM) and the interstellar medium (ISM) of the galaxy, or gravitative interactions between the cluster members, can lead to a gradual cessation of star formation.

Environmental effects are expected to get stronger at $z < 0.5$ as the large-scale structures of the universe evolve (e.g. Fig. 15 Peng et al. 2010), and therefore clusters of galaxies at intermediate redshifts should be the ideal sites to observe these effects, which effectively lead to the quenching of star formation and are to some extent expected to also affect the gas metallicities of cluster galaxies. For example, both Pasquali et al. (2012) and Peng & Maiolino (2014) studied central and satellite SDSS galaxies and found that the average metallicity of satellite galaxies is higher than that of central galaxies, especially at low stellar masses. These latter authors speculated that low-mass satellite galaxies that have a weaker gravitational potential than their massive counterparts are more prone to environmental effects such as the ram pressure stripping of the hot halo gas (strangulation). Cooper et al. (2008) investigated a large sample of SDSS galaxies and demonstrated that there exists a fairly tight relationship between metallicity and environment, with more metal-rich galaxies being found at regions of higher over-density. Maier et al. (2016) and Maier et al. (2019a) studied the $Z(M^*, \text{SFR})$ of members of the CLASH and LoCuSS clusters at $z < 0.5$ in comparison to a sample of field galaxies and observed more enhanced metallicities for low-mass cluster members residing in over-dense regions than for their counterparts residing at larger clustercentric radii and in the field. These enhanced metallicities were interpreted as the result of strangulation. There are also indications of strangulation in $z > 1$ cluster galaxies (e.g. Maier et al. 2019b). Strangulation, also known as “starvation”, is a mechanism that leads to the removal of the diffuse hot gas reservoir confined in the galaxy halo, while the cold gas-disc is left unperturbed. This means that star formation can continue until the internal gas reservoir is used up. Therefore, after the ram pressure of the ICM strips off the hot halo gas, there is a time delay until the system undergoes star formation quenching. As the inflow of pristine gas that dilutes the ISM is truncated, the metallicities of the retained gas increase before the system undergoes complete quenching (e.g. Maier et al. 2019a).

In another recent publication, Roberts et al. (2019) used X-ray observations for $z < 0.1$ clusters to study the effects of the ICM on the quenching of satellite galaxies and found that the fraction of quenched galaxies increases with the density of the ICM. Their results are consistent with the scenario in which cluster galaxies experience a slow quenching phase due to the removal of the hot gas confined in their halos followed by a rapid quenching mode associated with the removal of the cold gas component due to ram pressure stripping as the galaxies approach the cluster centre.

In this paper we further explore the environmental effects on gas regulation within galaxies by measuring (O/H) abundances in a very massive cluster – RX J2248–443 – at $z \sim 0.35$, and

by comparing them to chemical abundances of field galaxies at similar redshifts. We investigate two connected relations, namely the MZR and the mass–sSFR relation, to establish whether they have an environmental dependency. The chemical abundances were derived from several diagnostics based on strong emission lines (ELs) such as: $H\beta$, $[\text{OIII}]\lambda 5007$, $H\alpha$, and $[\text{NII}]\lambda 6584$. At higher redshifts ($z \sim 0.5$), these ELs are shifted out of the wavelength range of optical spectroscopic surveys, with $H\alpha$ and $[\text{NII}]\lambda 6584$ falling at near-infrared wavelengths, and therefore requiring near-infrared spectroscopy to observe them. The epoch we probe ($z < 0.5$) is therefore the highest redshift at which all these ELs can be observed with the same optical spectrograph.

This paper is structured as follows: in Sect. 2 we present the selection of the cluster CLASH-VLT EL galaxies at $z \sim 0.35$ and their VIMOS spectroscopy. We also introduce the comparison samples of field galaxies from CLASH-VLT and zCOSMOS. We investigate the stellar masses and the AGN contribution, and present the derivation of SFRs and gas-phase metallicities for the 121 cluster and 130 field galaxies that we observe. In Sect. 3 we present the mass–sSFR relation and the MZR for cluster and field galaxies at $z \sim 0.35$. We investigate how the dense cluster environment affects the chemical enrichment of the galaxies. In Sect. 4 we discuss whether the mechanism of ram pressure stripping of the hot halo gas can account for the observed metallicity trends implied by our results and we present a comparison with literature metallicity studies of the intermediate redshift universe. In Sect. 5 we summarise our conclusions.

Throughout this study, we have used the concordance Λ CDM cosmology with $H_0 = 70 \text{ km s}^{-1} \text{ Mpc}^{-1}$, $\Omega_0 = 0.25$, $\Omega_\Lambda = 0.75$. We assume a Salpeter Salpeter (1955) initial mass function (IMF) for all the derived stellar masses and SFRs. We also note that (gas phase) metallicity and abundance are used to denote oxygen abundance, (O/H), throughout this paper.

2. Data and measurements: cluster and field galaxies at $z \sim 0.35$

2.1. Cluster and field galaxies from CLASH-VLT

The CLASH RX J2248–4431 cluster (hereafter R2248), also known as Abell S1063, is a massive X-ray-luminous galaxy cluster at $z \sim 0.35$. The system was observed as part of the HST Frontier Fields project and also as part of the “Cluster Lensing And Supernova survey with Hubble” (CLASH, Postman et al. 2012) and CLASH-VLT survey (Rosati et al. 2014). Chandra X-ray observations of R2248 revealed a very high X-ray luminosity as well as a very hot intracluster gas with a temperature of up to $\sim 14.3 \text{ keV}$ (Gómez et al. 2012). Observations have also shown that the cluster members have high velocity dispersions in the range of over 1000 km s^{-1} . Both the high velocity dispersion and X-ray temperature suggest that Abell S1063 is a very massive cluster with an estimated mass, according to Gómez et al. (2012), of $M_{200} > 2.5 \times 10^{15} M_\odot$ that probably formed through a merger event.

The CLASH-VLT survey is the follow-up spectroscopic campaign of CLASH on 13 intermediate-redshift $-0.3 < z < 0.6$ – clusters accessible from the Very Large Telescope (VLT) at Cerro Paranal in the Atacama Desert of Chile. The survey had 225 h allocated for observations, with 200 h of multi-object spectroscopy and 25 h of pre-imaging primarily using the VIMOS spectrographs low-resolution LR-blue grism and the middle-resolution MR grism. The data set on which this work is based consists of 947 CLASH-VLT VIMOS spectra for both field galaxies around R2248 and cluster members. The galaxies span a redshift range

of $0.01 < z < 0.9$. The observations were obtained as part of the ESO large program 186.A-0798 (Rosati et al. 2014; Rosati et al., in prep.). The spectra were registered with the VIMOS spectrograph with an exposure time of 1 h, using four middle-resolution masks with 1 arcsec slits and a resolution of $R = 580$. The covered wavelength range is 4800–10 000 Å, thereby including ELs from [OII] λ 3727 to [N II] λ 6584 for $z < 0.5$ galaxies, and [OII] λ 3727 to [OIII] λ 5007 for $0.5 < z < 0.9$. The observations were carried out at a wavelength domain contaminated by only a few strong OH sky lines. The VIMOS slit-masks were designed as sets of four pointings, with one of the quadrants centred on the cluster core. The data reduction of 947 galaxy spectra and the redshift determination were done with the VIMOS Interactive Pipeline and Graphical Interface (VIPGI; Scodreggio et al. (2005)) software package by the CLASH-VLT team.

Additional observations for the CLASH-VLT target R2248 are archival imaging data provided by the ESO Wide Field Imager (WFI) of the 2.2 m MPG telescope of La Silla Observatory. We used a catalogue containing the observed UBVRIz magnitudes together with the errors for each filter for 636 field and cluster galaxies. The photometric data were corrected for galactic extinction according to Schlafly & Finkbeiner (2011).

In addition to the CLASH-VLT galaxies, we used a sample of zCOSMOS field galaxies with $0.373 < z < 0.413$ as a comparison to R2248 due to the low number of field galaxies with $0.3 < z < 0.4$ from our data set. This zCOSMOS sample corresponds to the one used as a comparison to the MACSJ0416 cluster in Maier et al. (2016).

For our metallicity study, we also used a local comparison sample of SDSS emission line galaxies in the redshift range $0.04 < z < 0.08$, as in Maier et al. (2016). AGNs and low-ionisation nuclear emission regions (LINERs) were excluded from the sample based on the BPT (Baldwin et al. 2013) diagnostic. We applied a signal-to-noise (S/N) threshold in $H\alpha > 10$ for this sample of local galaxies and computed the oxygen abundances using the O3N2 method of Kewley et al. (2013). Therefore, we point out that this sample is different from other local comparison SDSS samples often used in the literature, such as for example the sample of Tremonti et al. (2004).

2.2. EL fluxes

The EL fluxes of R2248 cluster members and field galaxies were measured interactively using the package *splot* in IRAF, adopting the same approach as described in Maier et al. (2016). We only measure the EL fluxes for the middle-resolution spectra, because in the low-resolution spectra only the [OII] λ 3727 EL is present, making the derivation of oxygen abundances impossible. The ELs of interest, namely [OII], $H\beta$, [OIII], $H\alpha$, and [NII], were each individually fitted with a single Gaussian profile. This was done by marking two positions, blueward and redward of the EL, which give the region to be fitted as well as the fixed linear continuum. Through this fitting procedure, we obtained a value for the centre, the continuum at the centre, the integrated flux, and the equivalent width. Except for the continuum, all the aforementioned parameters are based on the fitted analytic profiles. This procedure was applied three times for each EL of interest in order to derive the mean flux value and the errors of the flux measurement. The flux errors were dominated by systematic uncertainties in establishing the local continuum, which was conservatively estimated by exploring rather extreme possibilities.

When compared to theoretical values, the observed ratios of $\frac{H\alpha}{H\beta}$ constrain the degree to which the stellar atmospheric

absorption lines reduce the measured Balmer emission, as well as the amount of reddening induced by dust. Thereby, spectra with a high S/N are required. In the absence of very high-quality Balmer line measurements, statistical corrections have to be applied to the measured strength of the Balmer emission lines, particularly the $H\beta$ emission line. Following the recommendation of Kobulnicky et al. (1999), we assume an average underlying stellar absorption in $H\beta$ of 3 ± 2 Å and correct the equivalent width of the spectral line by this amount, thereby increasing the $H\beta$ line flux. This correction is needed mainly when the EL is weak compared to the continuum. Such corrections of the $H\beta$ EL flux are often used in the literature for data at similar redshifts and with similar spectral resolution as the one used in this study (e.g. Maier et al. 2005, Maier et al. 2016). Quality flags were assigned to all the 947 investigated galaxy spectra. If a spectrum is described by a quality flag $f = 1$, this indicates that all the EL fluxes could be measured. If a spectrum is described by a quality flag $f = 2$, then the measurement of one EL flux was problematic: either the EL was very weak or the respective line was an artefact due to sky-lines. If a quality flag $f = 3$ is assigned to a spectrum, then two or more EL fluxes could not be measured. Most galaxies described by a quality flag $f = 3$ are earlier-type galaxies showing few or no ELs.

A consistency check on the EL flux measurements was done by comparing the IRAF measurements to the measurements offered by “Fitting Analysis using Differential Evolution Optimisation” (FADO, Gomes & Papaderos 2017), which is a tool specially designed to perform population spectral synthesis to derive different physical parameters from a galaxy spectrum, including EL fluxes. It is worth mentioning that the fluxes offered by FADO are corrected for underlying stellar absorption. We find good agreement between the measurements offered by the two different tools. Nevertheless, we chose to use the IRAF flux measurements as FADO had problems fitting the template spectral energy distributions for more than half of the provided spectra, due to the high quality requirements which were not met with middle-resolution observations. The flux measurements are given in Table A.1.

2.3. Selection of the cluster and field galaxies for our metallicity study – Phase space diagram

Position–velocity diagrams offer great insight into the orbital histories of the cluster members. The location of galaxies in such projected phase space diagrams (clustercentric radius vs. line-of-sight velocity) provides information about the accretion history of the systems. Virialised galaxies that have been in the cluster for a few crossings will accumulate at low clustercentric radii and will have on average low velocities. The infalling or recently accreted cluster galaxies will be found at higher velocities overall, and will therefore be spatially separated from the accreted members. Different recent studies have used such phase-space diagrams in order to probe both the kinematics and the accretion epochs of the cluster members, as well as to constrain the density and mass profile of the cluster (e.g. Jaffé et al. 2015; Capasso et al. 2019; Haines et al. 2015).

The R2248 members were identified from the clustercentric radius vs. line-of-sight velocity plane as lying within the “trumpet”-shaped caustic profile expected for galaxies infalling into the system and subsequently orbiting within the massive virialised structure; therein the mass model of Carlberg et al. (1997) was adopted. This method is based on a theoretical model which assumes that clusters are singular isothermal spheres. The

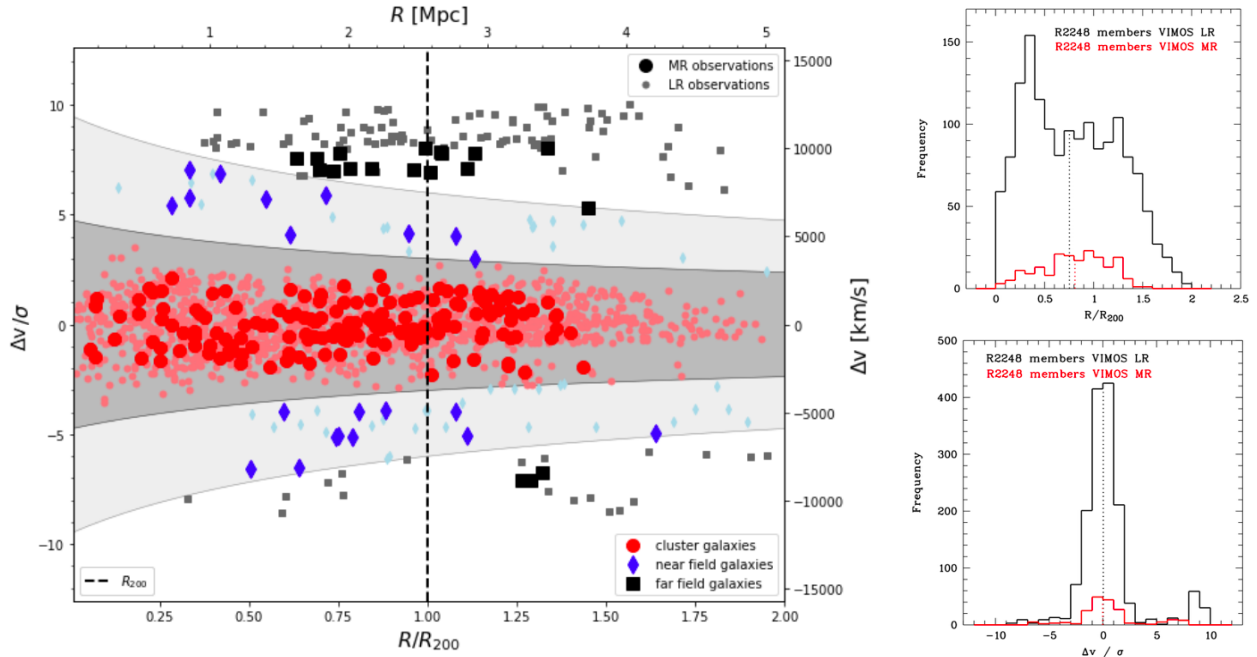


Fig. 1. *Left:* clustercentric radius vs. line-of-sight velocity for the sample of CLASH galaxies with $0.3 < z < 0.4$. Both galaxies with middle-resolution and low-resolution observations are shown. The red points which fall within the 3σ contours of the trumpet-shaped caustic profile (dark-grey area) are classified as R2248 cluster galaxies. The blue diamonds located between 3σ and 6σ (light-grey area) contours are considered to be galaxies from the near field, whereas the black squares located beyond the 6σ contours of the caustic are classified as far-field galaxies. Only the red symbols are considered for the computation of the cluster specific parameters such as R_{200} and M_{200} . The dashed black line shows R_{200} . The large symbols represent the galaxies with middle-resolution observations while the small ones represent the galaxies observed with a low-resolution grism, for which no flux measurements of ELs other than [OII] are available. *Right-top:* histogram showing the clustercentric radius normalised to R_{200} for the R2248 cluster members with low-resolution observations (black) and middle-resolution observations (red). The dotted lines show the median value for $\frac{R}{R_{200}}$ of both samples, colour coded accordingly. *Right-bottom:* histogram showing Δv normalised to the clusters velocity dispersion σ for the R2248 cluster members with low-resolution observations (black) and middle-resolution observations (red). The dotted lines represent the median values for $\frac{\Delta v}{\sigma}$ of both samples, colour coded accordingly.

mass model works as follows: first, the difference in velocity Δv between the mean velocity of the cluster $c\bar{z}$ and the velocity of each individual galaxy is computed. Subsequently, the values of Δv are normalised to the velocity dispersion σ of the cluster and are plotted against the projected clustercentric radius of the individual members in units of R_{200} . The parameter R_{200} represents the radius where the density is 200 times the mean density of the universe at the redshift of the cluster. The velocity dispersion profile used to mark the caustics within this model is calculated as follows: $\sigma^2 = B \cdot \frac{c_1 r / (1 + c_1 r) + c_2}{1 + r/b}$ where $B = 1/4$ and $b = 0.66$ are two parameters adjusted to fit the observed projected velocity dispersion at R . The c_1 and c_2 parameters are fixed at values of 0 and 1, respectively. This model is used to mark the 3σ and 6σ contours in the $\Delta v/\sigma - R/R_{200}$ plane, which separate between cluster members located within the 3σ contours of the caustic profile, and field galaxies located beyond 3σ (see more details in Carberg et al. 1997). This theoretical model was implemented in a python code, and for the computation of the cluster specific parameters we used the entire R2248 catalogue, which includes both the low-resolution and middle-resolution spectra. We only used the galaxies from the R2248 catalogue that have reliable redshift estimates based on the secure identification of at least two spectral features, that is, absorption and emission lines.

The left hand side of Fig. 1 shows the phase-space diagram for all galaxies from the R2248 catalogue with redshifts of $0.3 < z < 0.4$. The red points located within the 3σ contours of the caustic profile (dark-grey area) are classified as being members of the R2248 cluster. The blue diamonds, located between

3σ and 6σ (light-grey area) are classified as galaxies from the near field, while the black squares located beyond 6σ (white area) are considered to be far-field galaxies. The small faintly coloured symbols show the galaxies that have low-resolution observations while the larger, brighter ones show the galaxies for which there are middle-resolution observations, namely the data sample on which this work is based. The low-resolution spectra are not suited for a metallicity study, as only the [OII] $\lambda 3727$ EL is present in these spectra, making the derivation of oxygen abundances impossible. The dashed black line in the phase space diagram represents R_{200} .

The top panel from the right-hand side shows the distribution of the R2248 galaxies with middle-resolution (red) and low-resolution (black) spectra according to their clustercentric radius normalised to R_{200} . The dotted lines give the median values of the clustercentric distances of the two samples, colour coded accordingly. Our subsample of middle-resolution R2248 galaxies shows a similar distribution to the parent low-resolution sample, but the middle-resolution observations only reach a maximum clustercentric radius of $R = 1.5 \cdot R_{200}$ in contrast to the low-resolution observations which cover larger clustercentric radii of $R = 2 \cdot R_{200}$. The distribution of cluster members for which low-resolution observations are available however peaks at a clustercentric distance of $\sim 0.3 \cdot R_{200}$, whereas the distribution of cluster members identified with the middle-resolution observations peaks at a clustercentric distance of nearly R_{200} . This can be explained by the fact that the low-resolution observations were designed to observe mostly the crowded central region

of the cluster in order to identify passive members as well as gravitationally lensed galaxies. Due to the high multiplexing capacity of the VIMOS low-resolution mask, these observations allowed more redshift estimates in the central region of the cluster compared to the middle-resolution mask. The middle-resolution follow-up observations were designed in only a few pointings spread around the field of R2248.

The bottom panel from the right-hand side shows a histogram with the distribution of Δv , normalised to the clusters velocity dispersion σ for the R2248 cluster members with low-resolution observations (black) and middle-resolution observations (red). The median values for $\frac{\Delta v}{\sigma}$ for the two samples are given as the dotted lines, colour coded accordingly. The subsample of middle-resolution observations shows a fairly similar distribution to the parent sample of low-resolution spectra in the $\frac{\Delta v}{\sigma}$ space.

According to this mass model, the R2248 cluster can be described by the following parameters: $z_{\text{cluster}} = 0.3457 \pm 0.0001$, approximately 1361 members, $R_{200} = 2.57 \pm 0.05$ Mpc, $R_{500} = 1.71 \pm 0.05$ Mpc, $M_{200} = 1.77 \pm 0.03 \times 10^{15} M_{\odot}$, and $\langle v \rangle = 1180.916 \pm 40$ km s $^{-1}$. The errors for the cluster parameters were computed through the so-called Jackknife resampling method by subsequently removing a random subsample of approximately 200 galaxies from the R2248 catalogue containing both the low-resolution and middle-resolution observations and running the code several tens of times. The mean values and the errors for R_{200} , M_{200} , and $\langle v \rangle$ were then computed from the values offered by each run of the code with the reduced version of the R2248 catalogue. One should however keep in mind that these are just the random errors and do not represent the true uncertainties for the derived values of the cluster specific parameters.

The values for the cluster specific parameters are in fairly good agreement (within the errors) with other studies of R2248. Gómez et al. (2012) computed the mass of R2248 from the $M_{200}-\sigma_{\text{DM}}$ scaling relation and obtained the following values: $M_{200} = 3.97_{-0.9}^{+1.6} \times 10^{15} M_{\odot}$ and $R_{200} = 3.15 + 0.3$ Mpc, but based on only 51 cluster members for which they could measure the velocity dispersion. Melchior et al. (2015) studied the weak lensing masses and the galaxy distributions in massive clusters based on data from the Dark Energy Survey, and derived a radius for R2248 of $R_{200} \sim 2.2$ Mpc. On the other hand, Pizzutia et al. (2017) performed a maximum likelihood kinematic analysis on the RX J2248 cluster to determine the total mass profile in modified gravity models assuming a spherical Navarro–Frenk–White profile and obtained $R_{200} = 2.7 \pm 0.12$ Mpc. It is clear that different methods yield slightly different values for the cluster-specific parameters.

The investigated cluster galaxies with middle-resolution observations seem to be located, in projection, close to the cluster core. This is however not surprising, as the R2248 cluster is known to be one of the most massive CLASH clusters. The observations for the CLASH-VLT clusters were carried out by using 8–12 VIMOS pointings with one quadrant locked onto the core, and the data set on which this work is based corresponds to the observations from the crowded central region of the cluster, and therefore most galaxies do not reach the limits of the caustic profile.

The R2248 cluster galaxies span a redshift $0.33 < z < 0.36$, and from the parent middle-resolution sample of 947 galaxies, 178 have a redshift in the aforementioned range, of which only 61 have flux measurements for all ELs of interest (described by a quality flag $f = 1$). In order to have enough objects for the statistics, both $f = 1$ and $f = 2$ cluster galaxies are used throughout

this study, with our final sample consisting of 121 cluster members.

The comparison sample of CLASH field galaxies was restricted to the redshift range $0.3 < z < 0.4$ in order to avoid any biases with galaxy evolution, and only the $f = 1$ field galaxies were considered. As only 37 CLASH field galaxies with flux measurements for all ELs of interest are in the aforementioned redshift regime, an additional sample of 93 zCOSMOS field galaxies with $0.373 < z < 0.413$ from Maier et al. (2016) was used as a comparison to the R2248 cluster galaxies.

To select a sample of galaxies for the metallicity study, some constraints on the S/N were applied. The S/N in the $H\alpha$ line was set to be $S/N_{H\alpha} > 5$. For the [OIII], $H\beta$, [OIII], and [NII] emission lines, the S/N threshold was restricted to $S/N > 2$. The rest-frame equivalent widths of $H\beta$ and $H\alpha$ were chosen to be $\text{EW}(H\beta) > 2 \text{ \AA}$ and $\text{EW}(H\alpha) > 3 \text{ \AA}$. This results in 90% of our cluster galaxies having $S/N_{H\alpha} > 10$, and 10% having $5 < S/N_{H\alpha} < 10$.

2.4. Stellar masses

Stellar masses were derived using the code LePhare of Arnouts & Ilbert (2011), which fits stellar population synthesis models to the available photometry: the observed magnitudes in the WFI UBVRIz-bands. The code is composed of a set of FORTRAN commands, which incorporate the standard χ^2 minimisation method that offers the best match to a reference set of spectral templates for the given photometric data. The used population synthesis models are based on the galaxy library of simple stellar populations spectra from Bruzual & Charlot (2003), and the templates were fitted for stellar ages of between 1 and 11 Gyr. This premise was based on the fact that at $z \sim 0.35$, the universe was ~ 9.8 Gyr old and most of the stellar mass was assembled by that time. The redshift was kept fixed and we limited the number of extinction $E_{(B-V)}$ values (0.1, 0.3, and 0.5) in order to avoid over-fitting. The used cosmological parameters are in accordance to the Λ CDM model, and based on them, the code will reject models older than the age of the universe. The absolute magnitudes were derived in the reference band, chosen to be the R-band, from the apparent magnitude in the observed band, which was selected automatically to be as close as possible to the reference band, redshifted in the observer frame, in order to limit the template dependency. LePhare assumes a Chabrier IMF (Chabrier 2003) when deriving stellar masses. These Chabrier masses were then converted to Salpeter IMF (Salpeter 1955) masses according to Pozzetti et al. (2007), who found the factor of 1.7 to be a systematic median offset in the masses derived with the two different IMFs. This factor was also found to have a very small dispersion and a rather constant value for a wide range of SFHs. We are confident that the derived stellar masses are robust, since the $B - R$ colour encompasses the redshifted 4000 Å break and is thus sensitive to the galaxy mass-to-light ratios (e.g. Kauffmann et al. 2003b). The values for the stellar masses of the R2248 cluster galaxies are given in Table A.1.

2.5. Star formation or AGNs?

Using a set of four strong emission lines, [OIII], [NII], $H\alpha$, and $H\beta$, one can reliably distinguish between SF galaxies, Seyfert galaxies, LINERs and composite galaxies with both SF regions and an AGN. This diagnostic diagram (BPT diagram), which allows to assess whether the main source of ionisation is of stellar origin or is associated with AGN activity, was first introduced by

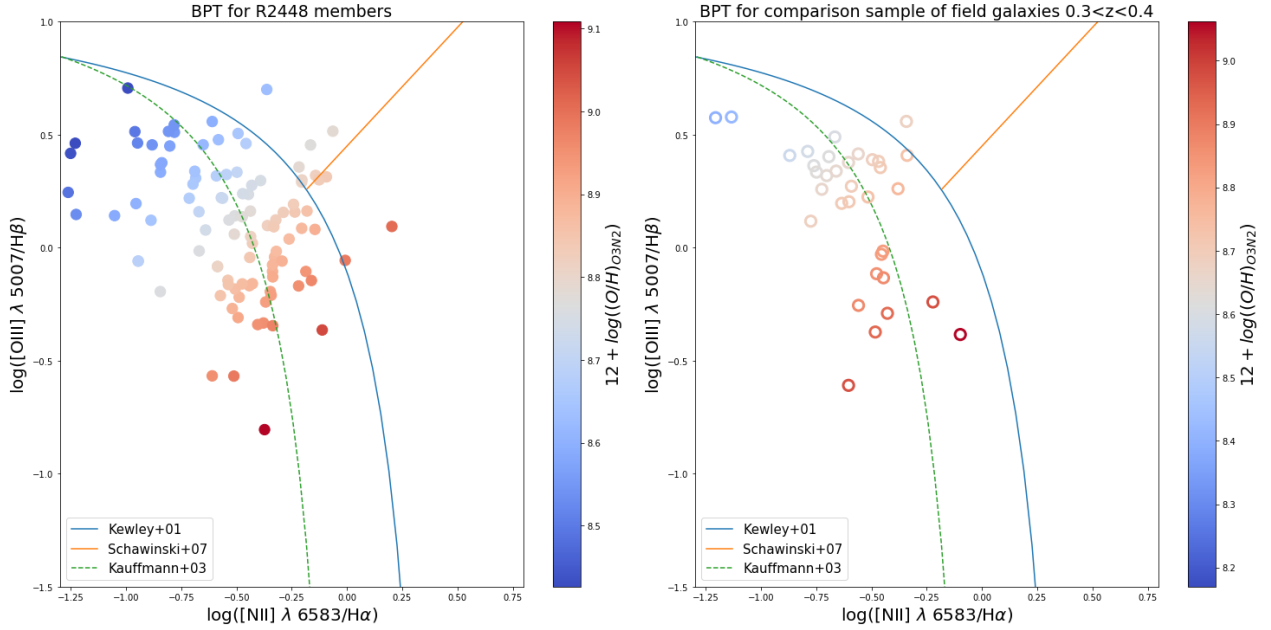


Fig. 2. BPT (Baldwin et al. 2013) diagram for the R2248 cluster members (*left*) and comparison sample of CLASH field galaxies with $0.3 < z < 0.4$ (*right*). This diagnostic diagram is used to distinguish whether the dominant source of ionisation comes from the stellar component or is rather associated with an AGN. The solid blue curve represents the theoretical curve of Kewley et al. (2001) and the green dashed one represents the empirical curve of Kauffmann et al. (2003a), which separate SF galaxies (below and left of the curves) from AGNs (above and right of the curves). The orange solid curve was derived by Schawinski & Thomas (2007) as the separation between Seyfert II galaxies (above and to the left) and LINERs (below and to the right). The colour bar shows the oxygen abundances of the investigated galaxies, as computed through the O3N2 method of Kewley et al. (2013). All CLASH galaxies classified as AGNs or LINERs were excluded from the sample.

Baldwin et al. (2013). The panel from the left-hand side of Fig. 2 shows a BPT diagram for the R2248 cluster galaxies while the panel from the right-hand side shows the same but for the comparison sample of CLASH field galaxies with $0.3 < z < 0.4$. The blue solid curve in both diagrams represents the theoretical curve of Kewley et al. (2001) and the green dashed one the empirical curve of Kauffmann et al. (2003a), which separate SF galaxies from AGNs. The orange solid curve of Schawinski & Thomas (2007) depicts the separation curve between Seyfert II galaxies and LINERs. If galaxies lie above and to the left of the three curves, and have high values in both [NII]/H α and [OIII]/H β , then they can be classified as Seyferts. If the galaxies lie above the two curves of Kewley et al. (2001) and Kauffmann et al. (2003a), and below the curve of Schawinski & Thomas (2007), and have high values only in [NII]/H α , then they are classified as LINERs. For galaxies that lie below and to the right of the two borderline curves of Kewley et al. (2001) and Kauffmann et al. (2003a), the main source of ionisation comes from the stellar component, making them SF galaxies. The area between these two curves represents the “uncertainty” region populated by composite galaxies with both active star formation and an AGN.

Most galaxies from our sample follow the SF sequence in the BPT diagnostic diagram, and all galaxies which are classified as Seyfert II or LINERs were excluded from the metallicity study (a total number of ten cluster galaxies and one CLASH field galaxy). According to Fig. 2 of Maier et al. (2016), all the zCOSMOS field galaxies can be classified as SF galaxies, and therefore none were excluded from the metallicity study.

2.6. Star formation rates

The SFRs for both the cluster members and the comparison sample of field galaxies were computed from the extinction-corrected luminosity of the H α line.

The H α EL is one of the best-understood and most reliable SFR indicators, as this nebular emission arises directly from the recombination of HII gas ionised by the most massive O- and early B-type stars and therefore traces the star formation over the lifetimes of these stars. Only the most massive stars with masses $>10 M_{\odot}$ and lifetimes <20 Myr have a significant contribution to the ionising flux, so the ELs, which re-emit this luminosity, provide us with an instantaneous estimate of the SFR, independent of the previous star formation history. The luminosity of the H α emission line can be used to calculate the SFR, by applying the Kennicutt (1998) conversion:

$$\text{SFR}(M_{\odot} \text{ yr}^{-1}) = 7.9 \times 10^{-42} L(\text{H}\alpha) (\text{ergs s}^{-1}). \quad (1)$$

The intensities of ELs arising from gas nebulae are strongly affected by selectively absorbing material on the line of sight to the observer. Thus, the most important source of systematic error in H α -derived SFRs is the extinction induced by dust. In order to accurately estimate SFRs, the luminosity of the H α EL was corrected for extinction based on the Balmer decrement following the equations introduced by Brocklehurst (1971).

In order to account for the slit losses, as the VIMOS masks have slits of 1 arcsec, an aperture correction was applied to the derived SFRs. Each VIMOS spectrum was convolved with the WFI R-band filter and then this magnitude was compared to the observed R-band magnitude of the respective galaxy. The difference between the two magnitudes offers the aperture correction factor for each spectrum. For $\sim 90\%$ of the sample, the aperture correction factors have values of between 1 and 3. This correction assumes that both the H β line flux and R-band continuum were equally affected by the slit losses and that the EW of H α remains constant throughout the entire galaxy (see e.g. Maier et al. 2009).

The main advantages of this calibration are its high sensitivity and the direct proportionality between the luminosity of the

nebular emission and the SFR. The values for the sSFRs of the R2248 cluster galaxies are given in Table A.1.

2.7. Oxygen abundances

The oxygen abundances for the R2248 cluster members as well as for the comparison sample of field galaxies were computed by means of three empirically calibrated metallicity estimators based on the relative strengths of ELs: the calibration by Kewley et al. (2013) which uses the O3N2 index and the calibrations derived by Maier et al. (2016) for SF galaxies using the [OIII]/H β and the [NII]/H α EL ratios.

The O3N2 index was first introduced by Alloin et al. (1979) as:

$$\text{O3N2} = \log\left(\frac{([\text{OIII}]\lambda 5007/\text{H}\beta)}{([\text{NII}]\lambda 6583/\text{H}\alpha)}\right). \quad (2)$$

By means of stellar evolutionary synthesis and photoionisation models with chemical evolution measurements from cosmological hydrodynamic simulations, Kewley et al. (2013) derived the following empirical metallicity calibration based on the O3N2 index:

$$12 + \log(\text{O}/\text{H}) = 8.97 - 0.32 \cdot \text{O3N2}. \quad (3)$$

This calibration corresponds to the Pettini & Pagel (2004) O3N2 calibration for the Kewley & Dopita (2002) metallicity scale, with a difference in the normalisation factor of +0.24. As this calibration relies on ratios of ELs which are close in wavelength, no corrections for reddening or accurate flux calibrations of the spectra are needed.

Maier et al. (2016) derived two metallicity calibrations for galaxies on the SF sequence based on Eqs. (3) and (4) of Kewley et al. (2013). The calibration as a function of the line ratio [OIII]/H β is very useful as a metallicity indicator for high-redshifted galaxies which do not have measurements of the [NII] and H α ELs, and can be expressed as follows:

$$12 + \log(\text{O}/\text{H}) = 8.97 - 0.32 \cdot (\log([\text{OIII}]/\text{H}\beta) - 0.61 / (\log([\text{OIII}]/\text{H}\beta) - 1.1) + 0.08). \quad (4)$$

The (O/H) calibration as a function of the [NII]/H α line ratio is given by the following equation:

$$12 + \log(\text{O}/\text{H}) = 8.97 - 0.32 \cdot (1.1 + 0.61 / (\log([\text{NII}]/\text{H}\alpha) + 0.08) - \log([\text{NII}]/\text{H}\alpha)). \quad (5)$$

This equation is similar to the (O/H) calibration of Salim et al. (2015), which uses the re-calibrated N2 index and matches the Pettini & Pagel (2004) O3N2 metallicity calibration. It was however demonstrated that the N2 metallicity estimator saturates for high (O/H) values.

The derived (O/H)s for both cluster and field galaxies using the three different calibrations are in relatively good agreement with each other. Recent studies of blue (Bresolin et al. 2016) and red supergiants (Davies et al. 2017) have however demonstrated that the metallicity calibration yielding the most accurate absolute metallicities is the O3N2 calibration, and we have chosen to use this calibration throughout this study, when all four ELs of interest were present. The values for the (O/H)s of the R2248 cluster galaxies are listed in Table A.1.

3. Results: Mass–metallicity and mass–sSFR relations in cluster and field galaxies

In this section we present several aspects of galaxy evolution in different environments in the framework of the relations between

mass and sSFR and mass and gas-phase metallicity. We subdivide the samples to study the environmental effects of the cluster and field populations. In order to be able to perform a meaningful investigation, and considering our relatively small number of targets, we divide the galaxies into three mass bins, as in Maier et al. (2016):

1. the low-mass bin $8.3 < \log(M/M_{\odot}) < 9.2$ (50 R2248 cluster galaxies, 22 field galaxies);
2. the intermediate-mass bin $9.2 < \log(M/M_{\odot}) < 10.2$ (58 R2248 cluster galaxies, 66 field galaxies), well populated by both field and cluster galaxies; owing to the fact that in this mass bin the number of cluster and field galaxies is similar, we consider it to be the “mass complete” bin and therefore, the comparison between the different populations in terms of their sSFRs and (O/H)s is based on galaxies from this bin;
3. the high-mass bin $10.2 < \log(M/M_{\odot}) < 11.1$ (13 R2248 cluster galaxies, 40 field galaxies).

3.1. The sSFR–mass relation at $z \sim 0.35$

The sSFR–mass relation was first investigated by Noeske et al. (2007) for a sample of galaxies in the All-Wavelength Extended Groth Strip International Survey field with redshifts in the range $0.2 < z < 1.1$. The results of this study demonstrated that galaxies with reliable signs of star formation form an apparent sequence with a limited range of SFR values at a given stellar mass and redshift (a scatter of $\sigma < 0.35$ dex) and with $\log(\text{SFR}) \propto M^*$.

Figure 3 shows the sSFR–mass relation for the R2248 cluster members (filled circles) and for the comparison sample of CLASH and zCOSMOS field galaxies (open circles) with available measurements of the H α emission line. The red solid line represents the main sequence of SF galaxies for a redshift of $z \sim 0.4$, as derived by Peng et al. (2010) through the following equation: $\log(\text{sSFR}) = -0.24 \cdot \log(M^*) + 1.86$. We assumed a dependency of sSFR on mass as it was observed for SDSS galaxies in the local universe by Renzini & Peng (2015): $\text{sSFR} \propto M^{*\beta}$ with $\beta \sim -0.24$.

The red filled and blue open circles show the median values of the sSFRs of cluster and field galaxies, respectively. The “mass complete” sample in this study is represented by the intermediate bin ($9.2 < \log(M/M_{\odot}) < 10.2$). In this mass bin, the median sSFR values of both cluster and field galaxies are comparable given the errors. Figure 4 displays the offset of the sSFRs of R2248 cluster members (filled circles) and the comparison sample of CLASH and zCOSMOS field galaxies (open circles) to the main sequence of SF galaxies at a redshift of $z \sim 0.4$, as derived by Peng et al. (2010). The red filled and blue open symbols show the median values of ΔsSFR for cluster and field galaxies respectively.

The median values for the sSFRs of both field and cluster galaxies and the scatter of the data points are quite consistent with the MS relation at $z \sim 0.4$ and with the scatter predicted by Peng et al. (2010). By taking into account the mean error of the star formation estimation of ~ 0.3 dex, the vast majority of the field and cluster galaxies can be classified as MS SF galaxies. The error on the SFR was estimated through error propagation by taking into account the flux measurement errors of the H α and H β ELs together with the resulting error of the dust extinction from the Balmer decrement. The distribution of both populations in the mass–sSFR plane is comparable, especially in the intermediate-mass bin $9.2 < \log(M/M_{\odot}) < 10.2$, where the two samples have a uniform coverage. Since only SF galaxies are considered within this work, no substantial differences between

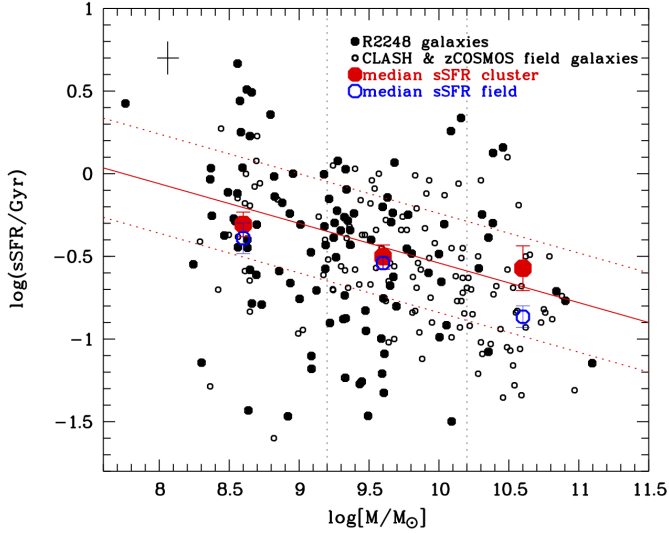


Fig. 3. sSFR– M relation for the R2248 cluster members (filled circles) and for the comparison sample of CLASH and zCOSMOS field galaxies (open circles) with available measurements of the $H\alpha$ emission line. Both $f = 1$ and $f = 2$ galaxies are considered. The median values of the sSFRs of cluster galaxies are plotted as the red symbols, while the blue, open symbols represent the median values of the sSFR of the field galaxies. The median sSFR values were computed for the three different mass bins, which are represented by the vertical dashed lines. The red solid line stands for the the main sequence of SF galaxies for a redshift of $z \sim 0.4$, as derived by Peng et al. (2010). The dashed red lines encompasses the 0.3 dex dispersion of the MS. The black cross in the upper left corner shows the mean error of the sSFR and mass estimation. In this study, the “mass complete” sample is represented by the intermediate bin ($9.2 < \log(M/M_{\odot}) < 10.2$). In this mass bin, the median sSFR values of both cluster and field galaxies are comparable given the errors.

the sSFRs of field and cluster galaxies can be observed. Therefore, the mass–sSFR relation of SF galaxies from this sample seems to be rather independent of whether the galaxies populate the field or cluster. These results are consistent with the findings of Maier et al. (2016) and Maier et al. (2019a), who find a similar distribution for members of CLASH and LoCuSS clusters and for field galaxies at $z < 0.5$ in the mass–sSFR plane.

3.2. Mass–metallicity relation at $z \sim 0.35$

The MZR determined from EL diagnostics was first introduced by Tremonti et al. (2004), who found a tight correlation of 0.1 dex between stellar mass and the gas-phase oxygen abundance, which extends over three orders of magnitude in stellar mass and a factor of ten in oxygen abundance.

Figure 5 shows the MZR for R2248 cluster members (filled circles) and the comparison sample of CLASH and zCOSMOS field galaxies (open circles) using the O3N2 metallicity calibration of Kewley et al. (2013). The magenta diamonds and curves represent the local SDSS relation. We selected a sample of emission line galaxies from the SDSS spectroscopic catalogues with $0.04 < z < 0.08$ as described in Maier et al. (2016). After excluding AGNs we recomputed the SDSS MZR using the O3N2 relation. The dotted magenta curves represent the 1σ scatter of this relation. The MZR for the SDSS sample was extrapolated down to lower masses of $\log(M/M_{\odot}) = 8.3$ by assuming that the slope remains constant for $\log(M/M_{\odot}) < 9$. The red filled and blue open circles give the median (O/H) values of

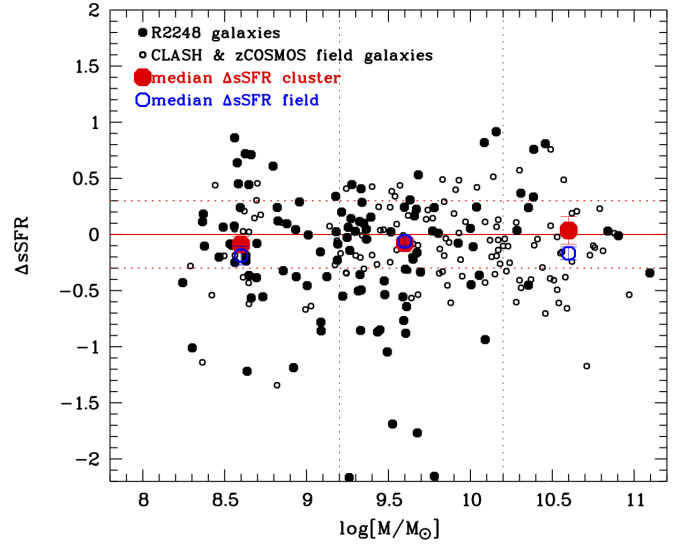


Fig. 4. Offset of the sSFRs of R2248 cluster members (filled circles) and the comparison sample of CLASH and zCOSMOS field galaxies (open circles) to the main sequence of SF galaxies at a redshift of $z \sim 0.4$, as derived by Peng et al. (2010). The red filled and blue open symbols indicate the median values of Δ sSFR for cluster and field galaxies respectively, as computed for the three different mass bins.

cluster and field galaxies, respectively. In the “mass complete” bin ($9.2 < \log(M/M_{\odot}) < 10.2$), the median (O/H) of the cluster galaxies is higher than the median (O/H) of the field galaxies by 0.065 dex, yielding a 1.8σ significance.

Figure 6 displays the offset of the gas phase metallicities of the R2248 cluster members (filled circles) and the comparison sample of CLASH and zCOSMOS field galaxies (open circles) to the local SDSS MZR, using the O3N2 metallicity calibration of Kewley et al. (2013). The red filled and blue open circles stand for the median value of the $\Delta(O/H)$ of cluster and field galaxies, respectively.

It is clear from these diagrams that both the cluster and field population at a redshift of $z \sim 0.35$ have chemical abundances that differ from the abundances of the local galaxies. However, the median value for the (O/H) of R2248 cluster and field galaxies from the intermediate- and high-mass bin is consistent with the 1σ scatter of the local MZR. The highest offsets to the local MZR occur for the cluster and field galaxies with the lowest masses ($8.3 < \log(M/M_{\odot}) < 9.2$), which generally show higher metallicities than the sample of galaxies from the local universe. The median value of the (O/H)s of both cluster and field galaxies at the low-mass end is higher than that of the SDSS sample by ~ 0.25 dex. However, at the highest masses ($10.2 < \log(M/M_{\odot}) < 11.1$) this trend is reversed, with most galaxies showing oxygen abundance values lower than those of the local SDSS sample by ~ 0.05 dex. When considering the “mass complete” bin $9.2 < \log(M/M_{\odot}) < 10.2$, cluster galaxies show more enhanced metallicities than their field counterparts, with a 1.8σ significance. This observed metallicity effect is investigated more thoroughly in the following section.

4. Environmental effects and tentative evidence for starvation

In this section we investigate whether or not the ram pressure stripping of the hot halo gas is a plausible mechanism to account

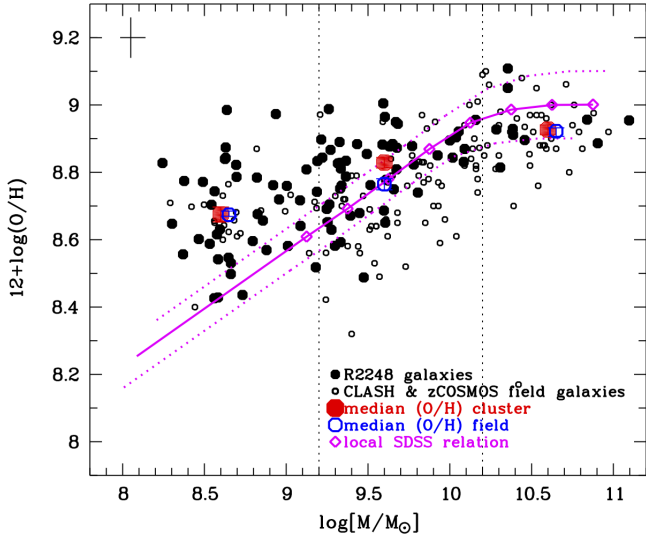


Fig. 5. Mass–metallicity relation for R2248 cluster members (filled circles) and the comparison sample of CLASH and zCOSMOS field galaxies (open circles) using the O3N2 metallicity calibration of Kewley et al. (2013). All cluster members and field galaxies with available measurements of the [OIII], H β , [NII], and H α lines are considered. The magenta diamonds and curves represent the local SDSS relation, consistently derived using the O3N2 calibration, with its 1σ scatter. The red filled and blue open circles show the median (O/H) values of cluster and field galaxies, respectively. The black cross in the upper left corner represents the mean error of the (O/H) and mass derivation. The vertical dashed lines show the three different mass bins, for which the median (O/H) values were computed, with the “mass complete” sample represented by the intermediate bin ($9.2 < \log(M/M_{\odot}) < 10.2$). In this mass bin, the median (O/H) for the cluster galaxies is higher than the median (O/H) for the field galaxies by 0.065 dex, with a 1.8σ significance.

for the enhanced metallicities of the cluster members from the “mass complete” bin, as compared to their field counterparts.

4.1. Mass–metallicity relation for cluster members with different accretion histories

In order to further explore the environmental effect on the gas regulation within galaxies, we compare the median (O/H) values of the CLASH and zCOSMOS field galaxies to the median (O/H)s of cluster members with different accretion histories. At clustercentric distances lower than $R_{500} \sim \frac{2}{3}R_{200}$, due to the high density of the ICM, cluster-specific hydrodynamical processes such as ram pressure stripping should be more effective in removing the hot diffuse halo gas from galaxies, especially if the galaxies have lower masses. Therefore, SF galaxies, which are found at distances of $R < R_{500}$, are expected to have more enhanced metallicities than their counterparts residing at larger clustercentric distances and in the field, in accordance with the findings of for example Maier et al. (2016) and Maier et al. (2019a). For this purpose, R2248 members located at $R < R_{500}$ were classified as “accreted” cluster galaxies and members residing at $R > R_{500}$ were classified as the “infalling” population.

The left hand side of Fig. 7 displays the clustercentric radius vs. line-of-sight velocity for the R2248 cluster members. The red symbols located at a clustercentric radius $R < R_{500}$ are considered to be accreted and possibly virialised cluster members, which are in dynamical equilibrium with the clusters’ gravitational potential. These systems were most probably accreted onto the cluster at earlier epochs, and the passive, quenched popula-

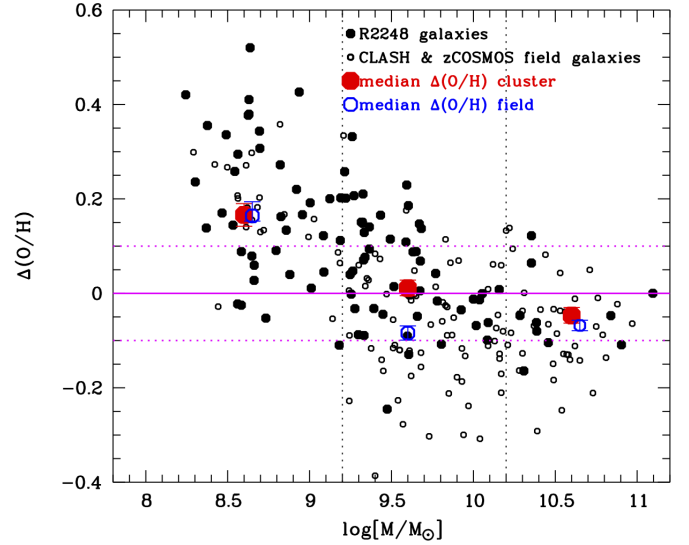


Fig. 6. Offset of the gas phase metallicities of the R2248 cluster members (filled circles) and the comparison sample of CLASH and zCOSMOS field galaxies (open circles) to the local SDSS MZR using the O3N2 metallicity calibration of Kewley et al. (2013). The red filled and blue open circles show the median value of the $\Delta(O/H)$ of cluster and field galaxies respectively, as computed for the three different mass bins.

tion probably passed through the apocentre of its first orbit. Haines et al. (2015) identified this population of “accreted galaxies” as galaxies that either formed locally or that were accreted as the core of the cluster was being assembled. The blue symbols located at a clustercentric radius of $R > R_{500}$ are classified as infalling galaxies, which have been just recently accreted onto the cluster. The ones showing high line-of-sight velocities are probably still on their first passage, and are not yet in dynamical equilibrium with the clusters’ gravitational potential. Some of these systems have probably just recently passed within R_{200} for the first time, but have not yet reached the pericentre. Therefore, the population of infalling galaxies shows higher line-of-sight velocities overall, as these systems are accelerated when they travel deep into the gravitational potential well of the cluster core. The smaller, fainter points represent the entire sample of CLASH VIMOS R2248 galaxies, which were observed with a low-resolution grism and for which no flux measurements are available.

The right-hand-side panel of Fig. 7 compares the MZR of the field galaxies (open black symbols), to the MZR of accreted (red symbols) and infalling (blue symbols) R2248 cluster members. To enable a meaningful comparison, only galaxies from the “mass complete” bin ($9.2 < \log(M/M_{\odot}) < 10.2$) are considered for this investigation. The median values for the gas phase metallicities of the three populations are shown as the large symbols, colour coded accordingly.

This investigation enables us to conclude the following: the median (O/H) value of the accreted cluster galaxies is higher than that of the infalling cluster galaxies by 0.04 dex, but due to the small sample sizes, this difference yields only a 0.8σ significance. On the other hand, the median (O/H) value of the accreted cluster galaxies is higher than that of the field population by 0.085 dex, yielding a 1.9σ significance. The distribution of the metallicities of $R < R_{500}$ galaxies is clearly shifted to higher values compared to their field counterparts.

Maier et al. (2016) and Maier et al. (2019a) observed a similar trend for other CLASH and LocuSS clusters, with galaxies at

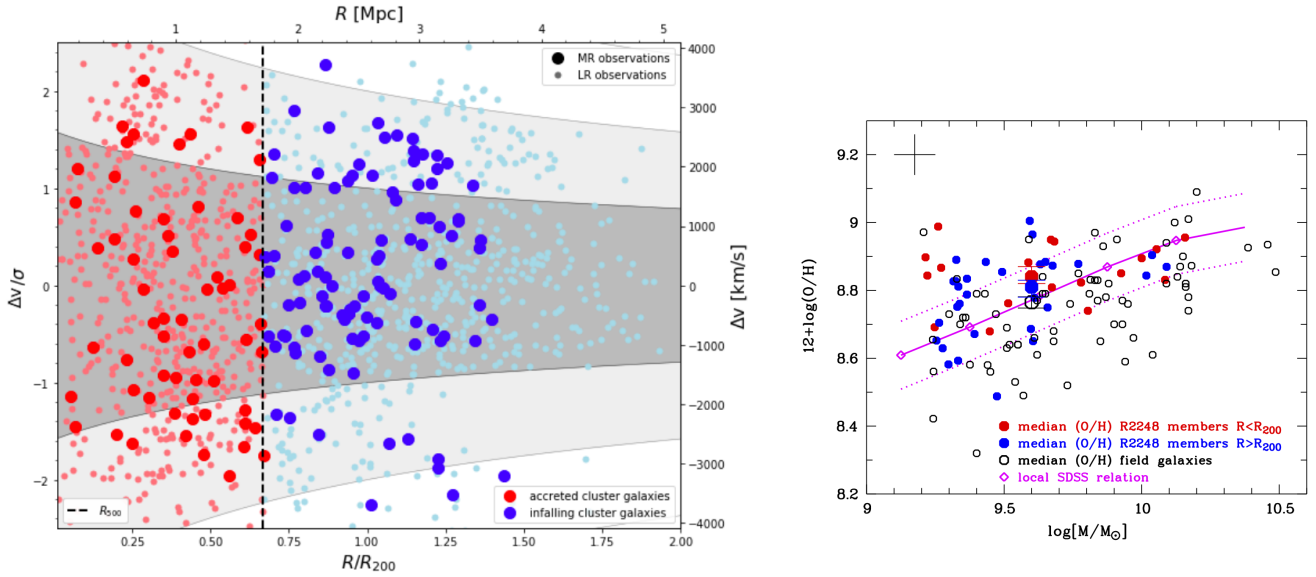


Fig. 7. *Left:* clustercentric radius vs. line-of-sight velocity for the R2248 cluster members. The red symbols located at a clustercentric radius $R < R_{500}$ are considered to be accreted and possibly virialised cluster members, which are in dynamical equilibrium with the clusters’ gravitational potential. The blue symbols located at a clustercentric radius $R > R_{500}$ are classified as infalling galaxies, which have been just recently accreted onto the cluster. The dashed black line stands for R_{500} . The large points represent the galaxies with middle-resolution observations, while the smaller, fainter points represent the entire sample of CLASH VIMOS R2248 galaxies, which were observed with a low-resolution grism. The dark grey-shaded region encompasses the 1σ contours of the caustic profile, while the light-grey shaded area encompasses the $1\sigma - 2\sigma$ contours. *Right:* MZR comparison between field galaxies, represented by the black open symbols, and the R2248 cluster members with different accretion histories: the red and blue symbols represent the accreted and infalling cluster members, respectively. Only galaxies from the “mass complete” bin ($9.2 < \log(M/M_{\odot}) < 10.2$) are considered. The median values for the gas phase metallicities of the three samples are shown as the large symbols, colour coded accordingly. The magenta curves and diamonds show the local SDSS relation as derived using the O3N2 calibration. The median (O/H) value of the accreted cluster galaxies is by 0.04 dex higher than that of the infalling cluster galaxies, and by 0.085 dex higher than that of the field galaxies.

smaller clustercentric radii showing more enhanced (O/H)s than galaxies located at larger clustercentric radii and in the field, and they concluded that infalling or recently accreted galaxies enhance their metallicities while travelling towards the cluster core. There are two possible scenarios to account for this: the systems either receive a metal-enriched gas inflow into their halo (e.g. Peng & Maiolino 2014; Gupta et al. 2018), or the gas inflow rate into the galaxy is suppressed (e.g. Pasquali et al. 2012). However, Maier et al. showed that the observed metallicity trends can be explained by strangulation.

4.2. The fundamental metallicity relation $Z(M^*, \text{SFR})$ for the $z \sim 0.35$ galaxies

As argued in the previous sections, it is clear that there exists a tight correlation between the SFR and the stellar mass of a galaxy (sSFR– M relation), as well as a correlation between the gas-phase metallicity of a system and its stellar mass (MZR). Observations have also shown that oxygen abundance anti-correlates with SFR, especially at low stellar masses, such that at a given mass, galaxies with high SFR show lower (O/H). This led to the conclusion that the chemical abundance of a galaxy is dependent on both the stellar mass and the SFR, giving rise to the so-called fundamental metallicity relation, $Z(M^*, \text{SFR})$.

For example, Mannucci et al. (2010) assumed that an inflow of gas is the responsible driver for the increase of the SFR and the dilution of the metallicity in order to explain the star formation as a second parameter in the MZR. Lilly et al. (2013) proposed a different explanation for the dependency of Z on M^* and SFR by introducing a simple model of galaxy evolution in which the SFR is regulated by the mass of gas present in a galaxy.

In this paper, we investigate whether at higher redshift and in a dense cluster environment, the $Z(M^*, \text{SFR})$ is similar to the one found in the local universe. For this purpose, we calculate the expected (O/H) values from the simple gas regulated model of Lilly et al. (2013) for each galaxy individually with their respective stellar mass and SFR. This is done by means of Eq. (40) from Lilly et al. (2013), which can be rewritten as follows:

$$Z_{\text{eq}} = Z_0 + y(1 - R)\text{SFR}/\Phi \quad (6)$$

where Z_{eq} is the equilibrium value for the metallicity, Z_0 is the metallicity of the infalling gas, y is the yield, R the fraction mass returned to the ISM, SFR the star formation rate, and Φ the gas inflow rate.

For example, Maiolino & Mannucci (2019) demonstrated that both the shape and the overall normalisation of the gas-phase MZR depend on the metallicity calibration used. Studies of blue (Bresolin et al. 2016) and red supergiants (Davies et al. 2017) have shown that the EL metallicity calibration yielding absolute metallicities is the O3N2 calibration, the one used throughout this work (cf. Fig. 15 from Maiolino & Mannucci 2019). Because of this, our measured metallicities should be well suited to comparison in an absolute way with the metallicities derived using the Lilly et al. (2013) bathtub model. To enable a meaningful comparison between theoretical models and observations, we compare our derived (O/H)s through the O3N2 method for galaxies from the “mass complete” bin to the predictions of Lilly et al. (2013). Figure 8 displays the difference between the measured (O/H)s using the O3N2 metallicity calibration and the expected (O/H)s from the FMR formulations of Lilly et al. (2013) for R2248 cluster galaxies (filled circles) and the comparison sample of field galaxies (open circles). We use a model

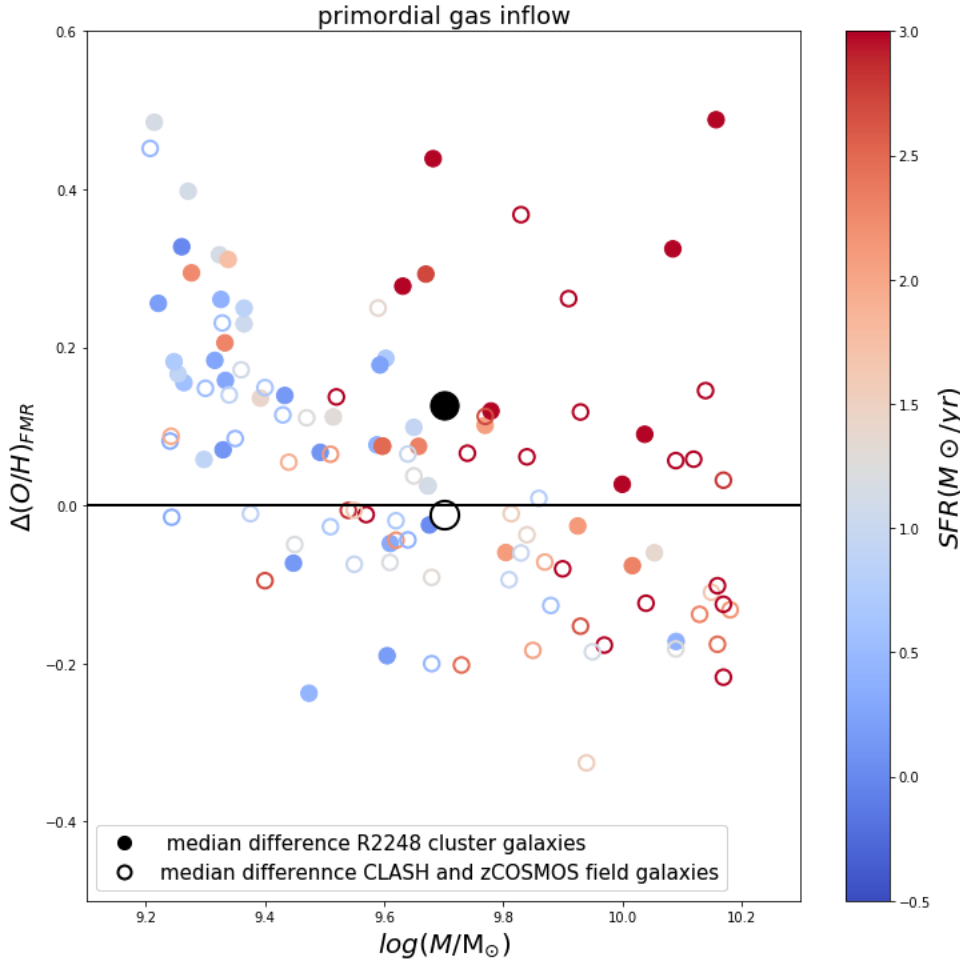


Fig. 8. Difference between the measured (O/H)s for R2248 cluster galaxies (filled circles) and the comparison sample of field galaxies (open circles), using the O3N2 metallicity calibration and the expected (O/H)s from the formulations of Lilly et al. (2013) for a primordial infall metallicity Z_0 relative to the yield y , $Z_0/y = 0$. As a third dimension, the SFRs of the investigated galaxies are shown in units of $[M_\odot \text{yr}^{-1}]$. The median values for the difference in (O/H) between measurements and predictions for both cluster and field galaxies are plotted as a reference and are represented by the large dark and large open circles respectively. The errors of the median are smaller than the symbols, and therefore cannot be seen in the plot. Only the galaxies from the mass complete bin ($9.2 < \log(M/M_\odot) < 10.2$) are considered for this investigation. In this bin, the (O/H)s of the cluster galaxies (big filled circle) deviate more strongly from the FMR model predictions (by ~ 0.12 dex) than the ones for the field galaxies (big open circle), which are in quite good agreement with the model predictions.

for primordial gas inflow: the metallicity of the infalling gas Z_0 relative to the yield y is taken to be $Z_0/y = 0$. The median values for the difference in (O/H) between measurements and predictions for both cluster and field galaxies are represented by the large dark and large open circles respectively.

The main results of the comparison between model and observations can be summarised as follows: at intermediate masses, field galaxies seem to be in good agreement with model predictions, showing a median deviation of -0.01 dex (big open circle in Fig. 8) from the expected (O/H) value. Cluster galaxies on the other hand deviate more strongly from the theoretical predictions, showing on average $+0.12$ dex (big dark circle in Fig. 8) higher gas-phase metallicities than predicted.

Our results are consistent with the findings of Maier et al. (2016) and Maier et al. (2019a) who studied the environmental effect on gas regulation within cluster galaxies and found that lower-mass cluster galaxies have higher metallicities than predicted by the models which assume an inflow of pristine gas, and that these systems also deviate more strongly from the FMR predictions than systems residing in lower density environments. This indicates that a strangulation scenario in which the gas inflow is cut off can explain the enhanced (O/H)s.

These findings are also in accordance with the predictions of Peng & Maiolino (2014), who studied the dependency of the MZR of SDSS galaxies on the environment with regards to both the over-density and central-satellite dichotomy. These latter authors find that for a given stellar mass, there is a fairly strong dependence of the gas phase metallicity on the density of the ICM, with high-metallicity galaxies (satellites) residing in

denser regions than their low-metallicity analogues. The authors proposed that the inflow of gas into the halo of a galaxy residing in a dense cluster environment should get progressively more metal enriched (meaning that Z_0 becomes higher), thus producing enhanced metallicities for low-mass cluster galaxies as compared to their field counterparts. They also tested their results by applying the gas-regulator model of Lilly et al. (2013) and find a good accordance with the models with metal-rich gas inflow (also in agreement with the findings of e.g. Gupta et al. 2018 and Schaefer et al. 2019). However, no physical mechanism was proposed by Peng & Maiolino (2014) to explain how a metal-enriched gas inflow can still occur for galaxies residing in dense cluster environments. An alternative mechanism was proposed, which can lead to the same effects of enhanced metallicities in lower-mass cluster galaxies, namely strangulation. However, this scenario was not further elaborated by these latter authors as they found the sSFRs of cluster and field galaxies to be similar. The same trend is observed for our investigated sample of galaxies.

Strangulation or starvation is a mechanism that causes the removal of the diffuse hot gas reservoir confined in the galaxy halo, while the gas disc is left unperturbed. This means that star formation can actually continue until the internal gas reservoir is used up. Therefore, after the removal of the hot halo gas, there will be a time delay until the system undergoes star formation quenching. Because of this, even if the SFRs of cluster and field galaxies are comparable, this does not mean that strangulation should be excluded as a mechanism which explains the observed enhanced metallicities of intermediate-mass cluster members, as compared to their field counterparts.

4.3. Discussion: environmental effects

In a recent study, [Haines et al. \(2013\)](#) investigated a large sample of LoCuSS cluster galaxies of intermediate redshifts in terms of the evolution of their star formation activity, and found that massive, actively SF galaxies, when accreted into high-mass clusters, are slowly quenched. Infalling spiral galaxies lose their gas reservoirs due to (mild) ram pressure stripping as they interact with the hot ICM and this results in a gradual decrease of their SFRs. The authors found that the SFRs of cluster galaxies decline exponentially on timescales of between 0.7 and 2.0 Gyr, and concluded that mechanisms such as ram pressure stripping and strangulation are responsible for quenching star formation on such long timescales.

This is in accordance with another recent study by [Jaffé et al. \(2015\)](#), who investigated the effects of ram pressure on stripping the HI gas from intermediate-redshift cluster galaxies from the BUDHIES survey. These latter authors found that ram pressure plays an important role in removing the gaseous reservoir of galaxies, and that this can happen during the first infall into the cluster. However, these galaxies are still able to continue forming stars from the remaining gas disc. They also conclude that the gas stripping occurs once the galaxies have approached the dense ICM core and/or have gained enough velocity to cross the “stripping” area in phase-space defined as the small clustercentric distances and/or high line-of-sight velocities. After this stripping process, galaxies are expected to “oscillate” in phase-space, until they accumulate towards the cluster core due to dynamical friction. During this time, it is expected that the galaxies exhaust their gas reservoirs, which in turn causes the quenching of star formation.

[Gunn & Gott \(1972\)](#) demonstrated that gas can be removed from galaxies if the ram pressure exceeds the restoring force per unit area (i.e. gravitational restoring force) exerted by the galaxy. Based on this, [Bahé et al. \(2013\)](#) studied the environmental effects which lead to star-formation quenching in cluster galaxies employing a suite of high-resolution cosmological hydrodynamic simulations. These latter authors analysed galaxies from simulated groups and clusters with a wide range of stellar masses in order to compute the density of the ICM and the ram pressure in clusters, and this allowed them to investigate how effective ram pressure can strip away the gas reservoirs of galaxies. They find a systematic reduction of both the hot and cold gas component and a decline in the SF fraction of galaxies with decreasing clustercentric distance. For massive clusters with $M \sim 10^{15} M_{\odot}$ (similar to the mass of the R2248 cluster), Bahé et al. estimated the typical values for the ram pressure and those for the restoring pressure of the cold gas and warm gas. When comparing the restoring pressure to the ram pressure near R_{200} , the latter is too low to strip the cold gas in the most massive galaxies, but is just sufficiently high to strip the hot halo gas from lower-mass systems. As the hot halo gas is less tightly gravitationally bound (by around two orders of magnitudes) than the cold gas component, ram pressure can strip it off more efficiently, meaning that even the most massive galaxies can be affected out to $\sim 2-3R_{200}$ in clusters and most low-mass systems are subject to sufficient ram pressure stripping of the hot halo gas even at large clustercentric distances of $5 \cdot R_{200}$.

The removal of the hot-gas component at $R > R_{200}$ due to strangulation will lead to a delayed decrease in the SFR of the system, as the cold gas disc remains unperturbed, and thus stars can continuously form until the gas reservoir is consumed. Strangulation is a slow mechanism which at first will not affect the SFR of the galaxy. However, as galaxies continue to move

through the hot ICM towards the dense cluster centre, the ram pressure increases to values which are comparable to the restoring pressure of the cold gas, such that the cold-gas component can also be stripped away. The removal of the cold-gas disc of a galaxy leads to a rapid phase of complete star formation quenching (see slow-then-rapid quenching scenario of [Maier et al. 2019a](#)).

Once the gas supply of a galaxy is cut off due to strangulation, the system can be described through a “closed-box model”. For example, [Maier et al. \(2006\)](#) explored which region of the parameter space could reproduce the constraints imposed by the metallicity–luminosity relation of both local and high-redshift galaxies based on a large grid of Pégase2 models. These latter authors analysed different models in which the gas supplies of the galaxies are cut off, and these systems continue to form stars in a closed-box-like environment. The tracks of these closed-box models have demonstrated that after the gas inflow is suppressed and eventually stopped, galaxies enhance their gas phase metallicities by a factor of ~ 0.2 dex on timescales of ~ 1 Gyr. According to these findings, cluster galaxies that experience strangulation can enhance their metallicities while travelling towards the central parts of the cluster.

The observational results of this work reveal enhanced metallicities for intermediate-mass cluster galaxies as compared to the population of field galaxies at similar redshifts. As the investigated R2248 cluster galaxies extend out to a maximum distance from the cluster centre of $\sim 1.5 \cdot R_{200}$, ram pressure stripping has probably already affected the hot halo gas of these systems. Because of this, no significant difference (a difference of 0.04 dex yielding only 0.8σ significance) can be observed between the (O/H)s of infalling and accreted cluster members, as both of these populations reside, in projection, close to the cluster core. However, as seen in Fig. 5, the combined population of accreted and infalling cluster galaxies shows a more enhanced gas-phase metallicity than the field galaxies, with a $\sim 1.8\sigma$ significance. This indicates that when accreted, cluster galaxies (especially lower-mass ones) are more prone to be affected by strangulation, and therefore they will increase their metallicities while moving through the hot ICM towards the central regions of the cluster. The observed metallicity effect is indeed weak, but this is also related to the fact that a low number of galaxies was used for the statistics. To conclude, ram pressure stripping of the hot halo gas can be considered as a plausible mechanism to account for the observed metallicity effects in cluster galaxies of intermediate redshift.

5. Summary and conclusion

We study the impact that the environment has on the $Z(M^*, \text{SFR})$ relation of both CLASH R2248 cluster members at $z \sim 0.35$ and of field galaxies with $0.3 < z < 0.413$ based on CLASH-VLT VIMOS spectroscopy. The main results can be summarised as follows:

1. SF galaxies and AGNs: We used the BPT diagnostic diagram to differentiate between the main sources of ionisation within galaxies. Both field and cluster galaxies are not dominated by AGNs, and they follow the SF sequence in the BPT diagram (Fig. 2).
2. sSFR– M relation: Both field and cluster galaxies can be classified as SF MS galaxies, with just a lower fraction of galaxies classified as starburst or passive systems. Field and cluster galaxies show a similar sSFR– M and we therefore conclude that this relation is independent of environment when considering only SF galaxies (Fig. 3).

3. MZR: Both field and cluster galaxies follow the MZR of local SDSS galaxies, with an offset of low-mass galaxies ($8.3 < \log(M/M_{\odot}) < 9.2$) towards higher metallicities than the local MZR. Cluster galaxies with $9.2 < \log(M/M_{\odot}) < 10.2$ show more enhanced metallicities than their field counterparts by ~ 0.065 dex, yielding a $\sim 1.8\sigma$ significance (Fig. 5).
4. Tentative evidence for strangulation: We find several indications for a strangulation scenario for cluster galaxies with $9.2 < \log(M/M_{\odot}) < 10.2$
 - (a) (O/H) comparison between field and cluster galaxies at different clustercentric radii: In the “mass complete” bin, cluster galaxies with $R < R_{500}$ show more enhanced metallicities than their counterparts residing at $R > R_{500}$, by 0.04 dex, but due to small sample sizes, this difference yields a 0.8σ significance, and thus their metallicities can be considered to be consistent. The fact that we observe no significant difference between the metallicities of accreted and infalling cluster members can be explained by the fact that the sample of cluster galaxies resides, in projection, close to the cluster core (all within $1.5 \cdot R_{200}$), meaning that cluster-specific processes such as ram pressure stripping have probably affected the hot halo gas of all these galaxies. On the other hand, the median (O/H) value of the accreted cluster galaxies is higher than that of the field population by 0.085 dex, yielding a 1.9σ significance (Fig. 7).
 - (b) FMR: In the “mass complete” bin, the measured (O/H)s of field galaxies seem to be in better agreement with the expected (O/H)s from the gas-regulated model of Lilly et al. (2013) than the (O/H)s of cluster galaxies, which deviate more strongly from the model predictions, by 0.12 dex (Fig. 8). This discrepancy between observed and predicted metallicities indicates that starvation can indeed be responsible for the enhanced metallicities of cluster galaxies.

To conclude, the observational results of this study favour the scenario in which ram pressure stripping is responsible for the removal of the hot halo gas of R2248 cluster galaxies with $9.2 < \log(M/M_{\odot}) < 10.2$, thereby increasing their (O/H)s. We should also mention that the observed metallicity effects are indeed weak, but this is also due to the fact that we had a low number of objects with middle-resolution observations, leading to lower statistical significance. All cluster members are located close to the cluster core and do not reach the outskirts of the caustic profile, and therefore a meaningful comparison between galaxies of different accretion histories could not be carried out.

Acknowledgements. We would like to express our deep gratitude to Amata Mercurio and Piero Rosati for providing us with both the VIMOS redshift catalogue and the WFI photometric catalogue for the R2248 cluster galaxies with middle resolution VIMOS observations. We also thank the CLASH-VLT team for the data reduction. Special thanks to José Manuel Perez Martinez for sharing his expertise regarding LePhare with us. We would also like to thank the anonymous referee for providing constructive comments and help in improving the manuscript.

References

Alloin, D., Collin-Souffrin, S., Joly, M., et al. 1979, *A&A*, 78, 200
 Arnouts, S., & Ilbert, O. 2011, *Astrophysics Source Code Library* [record ascl:1108.009]

Bahé, Y. M., McCarthy, I. G., Balogh, M. L., & Font, A. S. 2013, *MNRAS*, 430, 3017
 Baldwin, J. A., Phillips, M. M., & Terlevich, R. *PASP*, 93, 5
 Balogh, M., Eke, V., Miller, C., et al. 2004, *MNRAS*, 348, 1355
 Bresolin, F., Kudritzki, R.-P., Urbaneja, M. A., et al. 2016, *ApJ*, 830, 64
 Brinchmann, J., Charlot, S., White, S. D. M., et al. 2004, *MNRAS*, 351, 1151
 Brocklehurst, M. 1971, *MNRAS*, 153, 471
 Bruzual, G. & Charlot, S. 2003, *MNRAS*, 344, 1000
 Capasso, R., Saro, A., Mohr, J. J., et al. 2019, *MNRAS*, 482, 1043
 Carlberg, R. G., Yee, H. K. C., Ellingson, E., et al. 1997, *ApJ*, 462, 32
 Chabrier, G. 2003, *PASP*, 115, 763
 Cooper, M. C., Tremonti, C. A., Newman, J. A., & Zabludoff, A. I. 2008, *MNRAS*, 390, 245
 Daddi, E., Dickinson, M., Morrison, G., et al. 2007, *ApJ*, 670, 156
 Davies, B., Kudritzki, R.-P., Lardo, C., et al. 2017, *ApJ*, 847, 112
 Dressler, A. 1980, *ApJ*, 236, 351
 Elbaz, D., Daddi, E., Le Borgne, D., et al. 2007, *A&A*, 468, 33
 Ellison, S. L., Patton, D. R., Simard, L., et al. 2008, *ApJ*, 672, L107
 Gómez, P. L., Valkonen, L. E., Romer, A. K., et al. 2012, *AJ*, 144, 79
 Gomes, J. M. & Papaderos, P. 2017, *A&A*, 603, A63
 Gunn, J. E., & Gott, J. R. 1972, *ApJ*, 176, 1
 Gupta, A., Yuan, T., Torrey, P., et al. 2018, *MNRAS*, 477, 35
 Haines, C. P., Pereira, M. J., Smith, G. P., et al. 2013, *ApJ*, 775, 126
 Haines, C. P., Pereira, M. J., Smith, G. P., et al. 2015, *ApJ*, 806, 101
 Jaffé, Y. L., Smith, R., Candlish, G., Poggianti, B., Sheen, Y.-K., & Verheijen, M. 2015, *MNRAS*, 448, 1715
 Kauffmann, G., Heckman, T. M., Tremonti, C., et al. 2003a, *MNRAS*, 346, 1055
 Kauffmann, G., Heckman, T. M., White, S. D. M., et al. 2003b, *MNRAS*, 341, 33
 Kauffmann, G., White, S. D. M., Heckman, T. M., et al. 2004, *MNRAS*, 353, 713
 Kennicutt, Jr., R. C. 1998, *ARA&A*, 36, 189
 Kewley, L. J., Heisler, C. A., Dopita, M. A., et al. 2001, *ApJS*, 132, 37
 Kewley, L. J., & Dopita, M. A. 2002, *ApJS*, 142, 35
 Kewley, L. J., & Ellison, S. L. 2008, *ApJ*, 681, 1183
 Kewley, L. J., Dopita, M. A., Leitherer, C., et al. 2013, *ApJ*, 774, 100
 Kobulnicky, H. A., Kennicutt, Jr., R. C., & Pizagno, J. L. 1999, *ApJ*, 514, 544
 Lilly, S. J., Carollo, C. M., Pipino, A., et al. 2013, *A&A*, 577, 119
 Maier, C., Lilly, S. J., Carollo, C. M., et al. 2005, *ApJ*, 634, 849
 Maier, C., Lilly, S. J., Carollo, C. M., et al. 2006, *ApJ*, 639, 858
 Maier, C., Lilly, S. J., Zamorani, G., et al. 2009, *ApJ*, 694, 1099
 Maier, C., Ziegler, B. L., Lilly, S. J., et al. 2015, *A&A*, 577, A14
 Maier, C., Kuchner, U., Ziegler, B. L., et al. 2016, *A&A*, 590, A108
 Maier, C., Ziegler, B., Haines, C. P., et al. 2019a, *A&A*, 621, A131
 Maier, C., Hayashi, M., Ziegler, B., et al. 2019b, *A&A*, 626, A14
 Mannucci, F., Cresci, G., Maiolino, R., Marconi, A., & Gnerucci, A. 2010, *MNRAS*, 408, 2115
 Maiolino, R., & Mannucci, F. 2019, *A&ARv*, 27, 3
 Melchior, P., Suchyta, E., Huff, E., et al. 2015, *MNRAS*, 449, 2219
 Noeske, K. G., Weiner, B. J., Faber, S. M., et al. 2007, *ApJ*, 660, 43
 Pasquali, A., Gallazzi, A., & van den Bosch, F. C. 2012, *MNRAS*, 425, 273
 Peng, Y., & Maiolino, R. 2014, *MNRAS*, 438, 262
 Peng, Y.-J., Lilly, S. J., Kovač, K., et al. 2010, *ApJ*, 721, 193
 Peng, Y.-J., Lilly, S. J., Renzini, A., & Carollo, M. 2012, *ApJ*, 757, 4
 Pérez-Montero, E., Contini, T., Lamareille, F., et al. 2013, *A&A*, 549, A25
 Pettini, M., & Pagel, B. E. J. 2004, *MNRAS*, 348, 59
 Pizzutia, L., Sartoris, B., Amendola, L., et al. 2017, *JCAP*
 Postman, M., Coe, M., Benitez, N., et al. 2012, *ApJS*, 199, 25
 Pozzetti, L., Bolzonella, M., Lamareille, F., et al. 2007, *A & A*, 474, 443
 Renzini, A., & Peng, Y. 2015, *ApJ*, 801, 29
 Roberts, I. D., Parker, L. C., Brown, T., et al. 2019, *ApJ*, 873, 42R
 Rosati, P., Balestra, I., Grillo, C., et al. 2014, *The Messenger*, 158, 48
 Salim, S., Lee, J. C., Ly, C., et al. 2014, *ApJ*, 797, 126
 Salim, S., Lee, J. C., Dave, R., & Dickinson, M. 2015, *ApJ*, 808, 25
 Salpeter, E. E. 1955, *ApJ*, 121, 161
 Schawinski, K., & Thomas, D. 2007, *MNRAS*, 382, 1415
 Schaefer, A.L., Tremonti, C., Pace, Z., et al. 2019, *ApJ*, 884, 156
 Schlafly, E. F., & Finkbeiner, D. P. 2011, *ApJ*, 73, 103
 Scodreggio, M., Franzetti, P., Garilli, B., et al. 2005, *PASP*, 117, 1284
 Whitaker, K. E., Franx, M., Leja, J., et al. 2014, *ApJ*, 795, 104
 Tremonti, C. A., Heckman, T. M., Kauffmann, G., et al. 2004, *ApJ*, 613, 898
 Zahid, H. J., Geller, M. J., Kewley, L. J., et al. 2013, *ApJ*, 771, L19

Appendix A: Catalogue

Table A.1. Catalogue for the RX J2248 cluster galaxies.

Galaxy	$F(\text{H}\beta)$	$F([\text{OIII}])$	$F(\text{H}\alpha)$	$F([\text{NII}])$	$\log(M/M_{\odot})$	$\log(\text{sSFR}/\text{Gyr})$	$12 + \log(\text{O}/\text{H})$
01	1.13 ± 0.12	2.77 ± 0.18	4.03 ± 0.15	1.28 ± 0.30	8.54	-0.29	8.70
02	* ± *	0.58 ± 0.10	* ± *	0.67 ± 0.08	9.57	*	*
03	* ± *	1.77 ± 0.25	* ± *	* ± *	10.61	*	*
04	2.07 ± 0.10	1.65 ± 0.08	7.56 ± 0.30	2.73 ± 0.12	9.59	-1.00	8.88
05	7.60 ± 0.40	7.82 ± 0.25	32.70 ± 0.70	3.71 ± 0.20	9.60	-0.20	8.69
06	2.46 ± 0.01	5.11 ± 0.21	8.21 ± 0.31	0.45 ± 0.30	9.47	-0.83	8.49
07	3.89 ± 0.19	4.09 ± 0.20	18.55 ± 0.30	8.70 ± 0.30	9.77	-0.45	8.88
08	* ± *	* ± *	0.60 ± 0.07	* ± *	9.38	*	*
09	2.79 ± 0.30	2.64 ± 0.20	49.65 ± 0.60	15.95 ± 0.90	10.39	0.13	8.91
10	* ± *	* ± *	0.54 ± 0.10	* ± *	9.56	*	*
11	0.71 ± 0.09	1.52 ± 0.15	2.64 ± 0.22	1.53 ± 0.30	9.22	-0.90	8.84
12	1.37 ± 0.17	2.09 ± 0.13	9.66 ± 0.30	4.21 ± 0.16	9.78	-0.25	8.82
13	* ± *	0.45 ± 0.10	0.64 ± 0.20	0.44 ± 0.05	9.32	*	*
14	* ± *	1.68 ± 0.03	2.11 ± 0.14	4.86 ± 0.20	10.56	*	*
15	0.79 ± 0.14	2.11 ± 0.20	2.89 ± 0.25	0.42 ± 0.15	9.01	-0.31	8.58
16	* ± *	* ± *	2.01 ± 0.34	2.30 ± 0.80	9.19	*	*
17	1.52 ± 0.22	1.10 ± 0.10	27.00 ± 0.40	11.30 ± 0.80	10.16	0.34	8.96
18	0.11 ± 0.03	0.28 ± 0.03	0.51 ± 0.27	* ± *	9.53	-2.11	*
19	1.45 ± 0.12	1.60 ± 0.10	10.60 ± 0.05	5.38 ± 0.65	10.00	-0.49	8.89
20	* ± *	* ± *	* ± *	* ± *	8.74	*	*
21	1.24 ± 0.14	1.13 ± 0.10	18.00 ± 0.50	7.70 ± 0.20	10.39	-0.30	8.93
22	1.29 ± 0.10	3.88 ± 0.10	3.64 ± 0.28	0.20 ± 0.07	8.73	-0.79	8.44
23	6.35 ± 0.30	11.15 ± 0.05	25.60 ± 0.60	16.85 ± 1.20	11.32	-2.05	8.86
24	0.94 ± 0.64	* ± *	5.89 ± 0.80	3.14 ± 0.32	9.35	-0.28	*
25	1.61 ± 0.11	2.42 ± 0.03	8.00 ± 0.22	1.83 ± 0.30	9.80	-0.48	8.74
26	3.73 ± 0.18	6.32 ± 0.08	16.30 ± 0.02	5.05 ± 0.25	9.51	-0.40	8.76
27	* ± *	* ± *	* ± *	* ± *	9.55	*	*
28	0.89 ± 0.08	0.78 ± 0.20	4.49 ± 0.29	2.92 ± 0.23	9.68	0.07	8.94
29	4.85 ± 0.50	1.47 ± 0.03	2.73 ± 0.13	0.84 ± 0.26	9.26	-2.53	8.99
30	1.14 ± 0.08	2.84 ± 0.11	3.86 ± 0.10	0.99 ± 0.20	9.45	-1.26	8.68
31	3.38 ± 0.28	6.70 ± 0.37	11.60 ± 0.03	3.12 ± 0.27	9.08	-0.48	8.72
32	0.23 ± 0.30	1.80 ± 0.50	2.86 ± 0.25	* ± *	9.18	-0.00	*
33	1.86 ± 0.40	1.67 ± 0.10	8.27 ± 0.38	5.70 ± 0.26	9.60	-0.75	8.96
34	0.91 ± 0.02	1.37 ± 0.07	2.86 ± 0.05	0.96 ± 0.01	8.38	-0.25	8.77
35	3.86 ± 0.23	5.86 ± 0.12	17.00 ± 0.50	5.25 ± 0.39	9.36	-0.34	8.79
36	* ± *	0.24 ± 0.18	* ± *	* ± *	9.92	*	*
37	* ± *	* ± *	* ± *	* ± *	9.68	*	*
38	4.19 ± 0.05	7.02 ± 0.20	15.45 ± 0.30	3.30 ± 0.03	9.26	-0.51	8.70
39	0.43 ± 0.02	0.40 ± 0.20	2.04 ± 0.20	0.55 ± 0.20	9.49	-1.46	8.85
40	0.83 ± 0.02	0.77 ± 0.01	1.50 ± 0.11	1.47 ± 0.21	8.64	-1.43	8.99
41	* ± *	0.22 ± 0.02	* ± *	* ± *	9.54	*	*
42	0.82 ± 0.12	1.51 ± 0.02	3.05 ± 0.17	0.34 ± 0.07	8.47	-0.37	8.60
43	0.08 ± 0.05	3.07 ± 0.06	* ± *	0.88 ± 0.02	8.18	*	*
44	0.16 ± 0.01	0.50 ± 0.05	1.79 ± 0.20	0.65 ± 0.09	9.61	-1.09	8.78
45	* ± *	* ± *	* ± *	* ± *	9.28	*	*
46	* ± *	* ± *	* ± *	* ± *	9.63	*	*
47	1.63 ± 0.28	6.19 ± 0.11	7.63 ± 0.40	1.87 ± 0.33	8.80	0.36	8.60
48	0.20 ± 0.05	* ± *	0.84 ± 0.07	0.84 ± 0.13	9.78	-2.64	*
49	0.43 ± 0.06	0.35 ± 0.02	1.17 ± 0.07	0.44 ± 0.04	9.43	-1.27	8.88
50	2.32 ± 0.20	6.03 ± 0.19	10.55 ± 0.50	1.51 ± 0.10	9.33	0.03	8.59
51	4.09 ± 0.14	9.80 ± 0.15	15.30 ± 0.30	3.16 ± 0.21	9.25	-0.30	8.65

Notes. The catalogue contains the fluxes of the ELs $\text{H}\beta$, $[\text{OIII}]$, $\text{H}\alpha$, $[\text{NII}]$ in units $10^{-17} \text{ erg s}^{-1} \text{ cm}^{-2}$ together with the errors of the flux measurements, the stellar mass as computed by LePhare, the SFR in units of $\log(\text{sSFR}/\text{Gyr})$, as computed using the luminosity of the $\text{H}\alpha$ EL and the oxygen abundance derived through the O3N2 method. Galaxy IDs, coordinates, and redshift will be available in a future publication (Mercurio et al., in prep.).

Table A.1. continued.

Galaxy	$F(\text{H}\beta)$	$F([\text{OIII}])$	$F(\text{H}\alpha)$	$F([\text{NII}])$	$\log(M/M_{\odot})$	$\log(\text{sSFR}/\text{Gyr})$	$12 + \log(\text{O}/\text{H})$
52	0.82 ± 0.08	2.17 ± 0.13	3.13 ± 0.12	0.63 ± 0.07	8.86	-0.59	8.66
53	0.22 ± 0.05	0.32 ± 0.10	2.98 ± 0.20	1.34 ± 0.12	10.05	-0.92	8.92
54	0.45 ± 0.08	0.25 ± 0.17	* \pm *	* \pm *	9.90	*	*
55	* \pm *	1.83 ± 0.19	18.50 ± 1.30	11.73 ± 1.10	10.46	*	*
56	0.20 ± 0.12	1.17 ± 0.11	2.25 ± 0.40	0.78 ± 0.10	8.83	-0.14	8.68
57	* \pm *	* \pm *	* \pm *	* \pm *	10.06	*	*
58	1.80 ± 0.08	3.78 ± 0.09	5.17 ± 0.30	1.85 ± 0.29	9.33	-1.23	8.75
59	0.95 ± 0.02	3.18 ± 0.13	3.92 ± 0.10	0.65 ± 0.03	8.37	0.03	8.56
60	1.29 ± 0.11	0.96 ± 0.09	5.89 ± 0.11	1.78 ± 0.16	9.33	-0.74	8.89
61	* \pm *	* \pm *	* \pm *	* \pm *	9.22	*	*
62	0.35 ± 0.09	0.23 ± 0.04	2.04 ± 0.20	0.94 ± 0.20	8.94	-0.66	8.97
63	2.89 ± 0.13	3.76 ± 0.27	13.55 ± 1.10	9.69 ± 0.33	9.21	-0.15	8.90
64	0.98 ± 0.32	1.06 ± 0.15	* \pm *	3.59 ± 0.40	9.35	*	*
65	* \pm *	0.77 ± 0.08	* \pm *	* \pm *	9.32	*	*
66	* \pm *	* \pm *	* \pm *	* \pm *	9.42	*	*
67	0.35 ± 0.02	1.02 ± 0.09	2.24 ± 0.20	0.50 ± 0.12	8.58	0.44	8.62
68	* \pm *	* \pm *	* \pm *	* \pm *	1.043	*	*
69	* \pm *	* \pm *	* \pm *	* \pm *	9.28	*	*
70	0.62 ± 0.03	0.56 ± 0.04	* \pm *	2.55 ± 0.70	9.25	*	*
71	* \pm *	* \pm *	* \pm *	* \pm *	10.65	*	*
72	* \pm *	* \pm *	15.60 ± 2.00	* \pm *	10.25	*	*
73	0.76 ± 0.07	0.81 ± 0.10	* \pm *	0.43 ± 0.04	8.33	*	*
74	0.59 ± 0.06	* \pm *	5.10 ± 0.40	* \pm *	10.60	-3.42	*
75	0.59 ± 0.05	1.45 ± 0.06	2.75 ± 0.32	* \pm *	8.56	-0.12	*
76	* \pm *	* \pm *	* \pm *	* \pm *	9.51	*	*
77	* \pm *	* \pm *	* \pm *	* \pm *	10.50	*	*
78	* \pm *	0.53 ± 0.06	1.19 ± 0.33	0.53 ± 0.20	8.97	*	*
79	0.80 ± 0.20	1.24 ± 0.20	6.45 ± 0.19	4.02 ± 0.14	9.63	-0.14	8.88
80	* \pm *	0.23 ± 0.03	* \pm *	* \pm *	9.02	*	*
81	0.75 ± 0.10	1.43 ± 0.04	2.83 ± 0.20	0.17 ± 0.10	8.66	-0.78	8.53
82	* \pm *	* \pm *	* \pm *	* \pm *	10.32	*	*
83	5.74 ± 0.13	3.25 ± 0.20	29.05 ± 0.55	11.45 ± 0.45	9.67	-0.24	8.95
84	0.56 ± 0.20	1.80 ± 0.18	31.10 ± 2.00	14.30 ± 0.50	10.46	0.16	8.90
85	1.61 ± 0.15	3.56 ± 0.08	6.56 ± 0.30	2.21 ± 0.13	9.19	-0.57	8.74
86	* \pm *	* \pm *	2.75 ± 0.20	2.63 ± 0.20	9.96	*	*
87	0.57 ± 0.10	0.63 ± 0.19	6.18 ± 0.30	2.85 ± 0.50	10.04	-0.30	8.90
88	0.67 ± 0.04	0.45 ± 0.06	0.95 ± 0.10	0.14 ± 0.01	8.92	-1.47	8.76
89	2.52 ± 0.33	4.95 ± 0.21	11.13 ± 0.80	3.04 ± 0.60	8.96	0.00	8.72
90	2.46 ± 0.08	6.71 ± 0.17	9.65 ± 0.30	1.38 ± 0.24	9.30	-0.34	8.58
91	1.14 ± 0.23	2.60 ± 0.30	2.90 ± 0.40	2.09 ± 0.52	8.69	-0.61	8.82
92	1.28 ± 0.10	1.56 ± 0.30	3.62 ± 0.26	1.35 ± 0.30	9.32	-0.88	8.83
93	* \pm *	* \pm *	* \pm *	* \pm *	9.58	*	*
94	0.26 ± 0.08	0.89 ± 0.18	2.06 ± 0.30	0.32 ± 0.10	8.65	0.23	8.55
95	0.73 ± 0.08	1.26 ± 0.08	3.70 ± 0.15	1.76 ± 0.15	9.32	-0.26	8.83
96	1.36 ± 0.13	0.56 ± 0.16	9.68 ± 0.30	* \pm *	10.00	-0.99	*
97	0.76 ± 0.13	0.70 ± 0.12	4.83 ± 0.13	1.57 ± 0.25	9.65	-0.68	8.88
98	1.72 ± 0.16	4.08 ± 0.12	5.91 ± 0.30	3.68 ± 0.30	9.33	-0.87	8.81
99	0.96 ± 0.10	1.99 ± 0.10	2.86 ± 0.11	1.06 ± 0.24	8.56	-0.44	8.74
100	* \pm *	* \pm *	* \pm *	0.61 ± 0.30	9.56	*	*
101	1.42 ± 0.10	4.89 ± 0.16	5.60 ± 0.10	0.61 ± 0.12	0.92	8.50	*
102	2.09 ± 0.05	7.13 ± 0.07	7.42 ± 0.10	2.20 ± 0.10	9.066	*	8.66
103	* \pm *	* \pm *	* \pm *	* \pm *	9.86	*	*
104	8.16 ± 0.19	5.42 ± 0.40	52.00 ± 1.00	16.00 ± 0.20	10.02	*	8.92
105	* \pm *	* \pm *	* \pm *	* \pm *	10.261	*	*
106	* \pm *	* \pm *	* \pm *	* \pm *	10.94	*	*
107	* \pm *	* \pm *	* \pm *	* \pm *	8.53	*	*
108	* \pm *	* \pm *	* \pm *	* \pm *	10.51	*	*
109	0.70 ± 0.15	2.25 ± 0.06	2.91 ± 0.10	1.99 ± 0.22	8.49	-0.11	8.77

Table A.1. continued.

Galaxy	$F(\text{H}\beta)$	$F([\text{OIII}])$	$F(\text{H}\alpha)$	$F([\text{NII}])$	$\log(M/M_{\odot})$	$\log(\text{sSFR}/\text{Gyr})$	$12 + \log(\text{O}/\text{H})$
110	* ± *	0.56 ± 0.08	* ± *	* ± *	9.61	*	*
111	1.50 ± 0.13	5.13 ± 0.16	13.60 ± 0.70	5.52 ± 0.15	9.66	-0.29	8.75
112	* ± *	* ± *	* ± *	1.44 ± 0.07	10.44	*	*
113	0.68 ± 0.12	1.66 ± 0.18	5.40 ± 0.50	4.35 ± 0.50	8.63	0.51	8.84
114	1.64 ± 0.10	1.44 ± 0.17	8.87 ± 0.13	2.56 ± 0.18	10.02	-0.65	8.84
115	0.73 ± 0.05	1.14 ± 0.13	2.90 ± 0.30	4.63 ± 0.30	9.59	-1.21	9.00
116	1.90 ± 0.18	4.52 ± 0.26	4.65 ± 0.09	0.95 ± 0.05	9.09	-1.10	8.64
117	3.65 ± 0.25	19.10 ± 0.20	14.75 ± 0.75	1.50 ± 0.20	8.56	0.67	8.43
118	1.07 ± 0.06	1.36 ± 0.08	4.87 ± 0.50	* ± *	8.93	-0.24	*
119	* ± *	* ± *	* ± *	* ± *	9.63	*	*
120	5.48 ± 0.30	11.10 ± 0.60	43.90 ± 0.90	25.10 ± 0.60	10.09	0.26	8.83
121	* ± *	0.15 ± 0.00	1.12 ± 0.23	2.64 ± 0.20	8.97	*	*
122	* ± *	* ± *	* ± *	1.37 ± 0.21	9.44	*	*
123	* ± *	* ± *	* ± *	* ± *	9.710	*	*
124	0.25 ± 0.03	0.50 ± 0.05	* ± *	* ± *	8.96	*	*
125	* ± *	* ± *	* ± *	* ± *	9.28	*	*
126	3.53 ± 0.20	3.82 ± 0.09	14.05 ± 0.20	3.64 ± 0.30	9.67	-0.62	8.81
127	* ± *	* ± *	* ± *	* ± *	9.27	*	*
128	3.26 ± 0.20	8.64 ± 0.12	13.70 ± 0.60	3.89 ± 0.80	9.25	-0.39	8.69
129	* ± *	* ± *	* ± *	* ± *	10.26	*	*
130	5.48 ± 0.28	4.26 ± 0.25	22.70 ± 0.50	7.08 ± 0.06	9.27	-0.22	8.87
131	1.01 ± 0.09	1.82 ± 0.09	2.94 ± 0.23	* ± *	9.09	-1.18	*
132	0.45 ± 0.05	0.78 ± 0.12	1.08 ± 0.07	0.14 ± 0.10	8.30	-1.14	8.65
133	1.00 ± 0.06	1.55 ± 0.20	3.42 ± 0.23	1.00 ± 0.08	9.00	-0.76	8.76
134	0.92 ± 0.09	3.33 ± 0.11	4.66 ± 0.16	1.22 ± 0.15	8.59	0.04	8.63
135	* ± *	* ± *	* ± *	* ± *	10.202	*	*
136	* ± *	0.48 ± 0.04	* ± *	1.22 ± 0.15	10.31	*	*
137	0.88 ± 0.40	3.12 ± 0.12	2.68 ± 0.20	0.44 ± 0.06	7.76	0.43	8.55
138	* ± *	* ± *	* ± *	* ± *	9.17	*	*
139	1.18 ± 0.20	3.87 ± 0.07	5.64 ± 0.20	0.63 ± 0.04	9.18	-0.32	8.52
140	0.51 ± 0.06	0.59 ± 0.09	1.68 ± 0.11	* ± *	8.65	-0.58	*
141	0.68 ± 0.13	1.13 ± 0.10	3.71 ± 0.19	1.73 ± 0.27	9.36	-0.43	8.83
142	1.09 ± 0.10	3.37 ± 0.12	3.45 ± 0.30	0.20 ± 0.03	8.58	-0.29	8.43
143	0.89 ± 0.10	2.32 ± 0.10	3.41 ± 0.20	2.13 ± 0.30	9.12	-0.71	8.81
144	11.55 ± 2.00	9.46 ± 0.40	44.55 ± 0.50	26.90 ± 1.40	11.10	-1.15	8.95
145	* ± *	0.27 ± 0.01	* ± *	* ± *	9.47	*	*
146	0.94 ± 0.10	1.28 ± 0.12	3.09 ± 0.20	1.69 ± 0.30	8.63	-0.40	8.87
147	0.65 ± 0.07	0.76 ± 0.04	2.68 ± 0.30	0.97 ± 0.03	8.63	-0.45	8.84
148	* ± *	* ± *	* ± *	* ± *	10.06	*	*
149	3.50 ± 0.15	10.40 ± 0.30	11.10 ± 0.40	1.75 ± 0.20	8.88	-0.18	8.57
150	1.45 ± 0.15	1.47 ± 0.40	8.66 ± 0.30	2.51 ± 0.21	9.93	-0.60	8.85
151	1.43 ± 0.18	2.53 ± 0.12	3.56 ± 0.30	* ± *	8.36	-0.03	*
152	2.35 ± 0.13	3.60 ± 0.30	10.70 ± 1.00	* ± *	9.70	-0.80	*
153	3.39 ± 0.21	1.59 ± 0.21	34.60 ± 0.90	8.49 ± 0.90	10.84	-0.71	8.96
154	7.06 ± 0.18	23.85 ± 0.25	22.85 ± 0.25	2.50 ± 0.20	8.66	0.49	8.50
155	0.92 ± 0.15	1.53 ± 0.20	3.07 ± 0.23	0.27 ± 0.08	8.53	-0.27	8.59
156	* ± *	0.36 ± 0.02	* ± *	* ± *	9.60	*	*
157	* ± *	0.90 ± 0.18	* ± *	* ± *	9.15	*	*
158	0.25 ± 0.02	1.53 ± 0.09	2.20 ± 0.08	0.95 ± 0.05	9.28	0.08	8.63
159	2.48 ± 0.24	2.64 ± 0.09	2.78 ± 0.15	1.33 ± 0.30	9.68	-2.23	8.87
160	* ± *	* ± *	* ± *	* ± *	10.12	*	*
161	* ± *	* ± *	* ± *	* ± *	10.08	*	*
162	0.88 ± 0.10	1.41 ± 0.10	2.00 ± 0.22	1.03 ± 0.15	8.24	-0.55	8.83
163	3.88 ± 0.22	5.79 ± 0.40	38.70 ± 0.40	17.80 ± 1.00	10.90	-0.77	8.89
164	0.50 ± 0.02	0.76 ± 0.01	3.49 ± 0.11	1.17 ± 0.16	10.09	-1.50	8.87
165	1.50 ± 0.09	1.96 ± 0.07	10.60 ± 0.30	2.27 ± 0.28	9.34	-0.10	8.76
166	1.25 ± 0.15	0.22 ± 0.06	9.38 ± 0.50	3.97 ± 0.50	10.35	-0.39	9.11
167	1.14 ± 0.12	2.90 ± 0.40	5.52 ± 0.40	4.13 ± 0.40	9.19	-0.43	8.83

Table A.1. continued.

Galaxy	$F(\text{H}\beta)$	$F([\text{OIII}])$	$F(\text{H}\alpha)$	$F([\text{NII}])$	$\log(M/M_{\odot})$	$\log(\text{sSFR}/\text{Gyr})$	$12 + \log(\text{O}/\text{H})$
168	3.01 ± 0.17	4.63 ± 0.30	24.70 ± 1.00	9.04 ± 0.32	10.31	-0.25	8.81
169	2.33 ± 0.15	3.18 ± 0.30	14.10 ± 0.60	7.72 ± 0.40	10.05	*	*
170	0.77 ± 0.08	2.38 ± 0.07	4.10 ± 0.20	0.54 ± 0.10	8.58	0.25	8.54
171	2.53 ± 0.13	2.10 ± 0.14	19.00 ± 0.70	8.61 ± 0.40	10.28	-0.57	8.93
172	1.70 ± 0.10	4.23 ± 0.10	5.29 ± 0.03	3.21 ± 0.18	8.70	-0.31	8.79
173	7.52 ± 0.28	14.10 ± 0.20	26.30 ± 0.50	5.08 ± 0.40	9.39	-0.24	8.67
174	0.59 ± 0.03	2.35 ± 0.10	3.13 ± 0.17	2.70 ± 0.50	8.82	-0.02	8.78
175	0.18 ± 0.06	* \pm *	1.83 ± 0.14	1.07 ± 0.13	9.48	-0.95	*
176	3.04 ± 0.30	2.31 ± 0.15	21.50 ± 0.60	16.60 ± 0.60	10.35	-1.08	9.05
177	1.94 ± 0.07	7.39 ± 0.30	6.04 ± 0.21	1.94 ± 0.24	9.61	-1.33	8.65
178	* \pm *	0.35 ± 0.03	* \pm *	* \pm *	9.44	*	*